

Understanding cyclic variability in a spark ignited engine using multi-cycle LES

O. Vermorel^{a,b,*}, S. Richard^a, O. Colin^a, C. Angelberger^a,
A. Benkenida^a and D. Veynante^c

^a*IFP, 1 & 4 Avenue de Bois-Préau, 92852 Rueil-Malmaison Cedex, France*

^b*now at CERFACS, CFD Team, 42 Avenue G. Coriolis, 31057 Toulouse Cedex
01, France*

^c*EM2C, CNRS and Ecole Centrale Paris, Grande Voie des Vignes, 92295
Châtenay-Malabry, France*

Abstract

Large-Eddy Simulation (LES) has been used to analyze the occurrence and the causes of cycle-to-cycle combustion variations in a spark-ignited four-valve single cylinder engine fuelled with a homogeneous propane-air mixture. The combustion modeling combines an Eulerian model derived from the RANS AKTIM model that mimics the spark ignition and the Extended Coherent Flame Model (ECFM-LES) that describes the flame propagation. The motion of piston and valves is accounted for using an Arbitrary Eulerian Lagrangian (ALE) technique with body-fitted meshes. The computation covers ten consecutive complete four stroke cycles. The obtained LES results are compared with experimental measurements. Although the number of computed cycles is fairly low, LES is shown to be able to reproduce both quantitatively and qualitatively the cyclic variability observed experimentally. The investigation of the possible causes of variability illustrates the unprecedented

possibility LES offers for understanding cycle-to-cycle variations.

Key words: Large-Eddy Simulation, Coherent Flame Model, cyclic variations, spark ignition, multi-cycle engine simulation

^{_____}
* Corresponding author.

Address: CERFACS, CFD Team, 42 Avenue G. Coriolis, 31057 Toulouse Cedex 01,
France.

Tel: +33 (0)5 61 19 30 33; fax: +33 (0)5 61 19 30 00.

Email address: `vermorel@cerfacs.fr` (O. Vermorel).

1 Introduction

Combustion in the cylinder of spark-ignition (SI) piston engines is characterized by an important level of cyclic variability. Instead of observing the same time evolution of the cylinder pressure for all cycles, a scatter of the individual cylinder pressure curves around the phase averaged mean appears. As a result, the work provided by each individual cycle differs from the mean work which is the design target of engine developers. In extreme cases partial burns or misfires may occur. A too large level of variability can have a negative impact on the drivability of the vehicle, and can lead to increased levels of pollutant emissions and fuel consumption. The review of Ozdor [1] suggests that the elimination of cycle-to-cycle variability could lead to a 10% increase in the power output for the same fuel consumption.

In the context of increasingly stringent restrictions on engine-out pollutant emissions, and of a strong demand for reducing the production of the greenhouse gas CO_2 , engine designers have introduced a number of new technology solutions. Among them, one can in particular cite fuel lean operation or increased dilution rates of the fresh charge by exhaust gas recirculation. Both these measures lead to a decrease in the laminar flame speed, which critically affects the flame propagation in the cylinder and may increase the magnitude of cycle-to-cycle combustion variations [2]. In this context cyclic variability may be seen as a first order nuisance which can considerably limit the range of operation of new engine combustion concepts. Predicting and controlling cyclic variability is thus an issue of prime necessity for today's engine designers.

Cycle-to-cycle combustion variations have been intensively studied over the last decades and a number of causes for their occurrence have been identified in SI engines [1–3]:

- variations of spark discharge characteristics;
- variations of in-cylinder mixture (overall fuel/air ratio and fraction of diluents);
- spatial mixture inhomogeneity at spark plug;
- variations of turbulence intensity;
- variations of mean flow speed and direction in the spark plug vicinity;
- variations of overall in-cylinder flow pattern.

However, the relative importance of these factors is not yet well established. All these phenomena are strongly coupled, dependent of the engine geometry or engine operation, and thus difficult to predict at the stage of the engine design. This is a major difficulty for automotive manufacturers since the unstable nature of an engine is often detected only late in the design cycle, when the costs of countermeasures are high.

Experimental techniques allow identifying and understanding the origins of cycle-to-cycle variations [4–7] but only an *a posteriori* analysis can be made. Despite the significant improvements of experimental techniques in the past years [8] experiments are still confronted to several problems linked to the difficulties related to piston engines:

- complexity of accurately controlling boundary conditions and operating conditions;
- restricted optical access to complex moving geometries that limits the ac-

curacy possible to obtain on very fine quantities;

- difficulties to isolate the different phenomena which are strongly coupled.

Numerical simulations represent a definitive complement as they can bring a new insight to predict cycle-to-cycle variations, allowing in theory both an *a priori* and an *a posteriori* analysis. Hereafter, 3D modeling aspects are focused on, keeping in mind that OD and 1D approaches are also interesting numerical alternatives that receive a growing interest from automotive industry.

Reynolds Averaged Navier-Stokes (RANS) is today's standard approach to 3D computational fluid dynamics (CFD) simulation of internal combustion (IC) engines' reactive flows [9]. It consists in resolving the phase or ensemble averaged Navier-Stokes equations, giving direct access to a mean engine cycle. Its moderate computational cost associated to globally good predictive capacities makes RANS simulation a powerful tool for industry, able to rapidly compare different design options and to give first tendencies. However, the RANS approach suffers from several inherent limitations. First, the prediction of complex phenomena like auto-ignition or pollutant emissions strongly depends on local instantaneous fields (composition, temperature) that can not be accurately predicted by mean quantities. Then, most RANS turbulence models as the well known and commonly used $k-\epsilon$ model [10] assume an isotropic turbulence so that the description of flows with strong anisotropy is inherently limited. Finally all intermittency effects due to large-scale motions like tumble precession [11] or to important deviations from the average like those caused by misfires or knock, can not be captured by such a method.

Large-Eddy Simulation (LES) can potentially overcome these inherent limitations of RANS. In LES a spatially localized filter is applied to a single realization of the studied flow. Resulting from this spatial filtering is a sepa-

ration between large scales (greater than the filter size and thus resolved on the grid) and scales smaller than the filter size which require modeling [12–15]. When applied to piston engine simulations LES thus predicts individual, spatially filtered cycles, and has therefore the potential to reproduce highly unsteady phenomena not accessible to RANS, like cyclic variations, misfires, knock, fast engine transients or engine start-up.

As often in CFD, the theoretical potential of a method is only a prerequisite which does not guarantee that it is practically applicable. A major limitation of LES when applied to industrial configurations has long been its high computational overload. In recent years, the development of massively parallel computers as well as CFD codes able to exploit them with high efficiency [16–18] has allowed LES to be performed in industrial configurations. LES of reactive flows in gas turbine combustors is an example where this technique has proven its unique capacity to predict unsteady effects like those related to interactions between acoustic waves and combustion [19–21]. Although the characteristics of IC engine flows seem particularly suitable for LES, the number of such simulations is still very limited. At first sight, this could seem surprising as the characteristic Reynolds number in piston engines is about a few thousands [22]. This means that the spectrum of spatial flow scales to be solved by LES is fairly moderate and does not necessitate huge computational grids. Some authors even suggest that typical RANS meshes ($\sim 10^5$ elements) would be sufficient to capture 80 – 90% of the flow’s kinetic energy [22,23]. Such a level of resolution seems largely reasonable for LES [14,24]. The important computational overload of a piston engine LES therefore does not come from the mesh size but instead from the important physical time that needs to be simulated. Indeed, many engine cycles are required in order to obtain a correct statistical representation of the flow.

In the last decade, several studies dealing with LES in engine configurations have been published. A first category concerns idealized or simplified engine configurations: steady flow rigs at fixed valve lift [25,26], compressed tumble flow in a square chamber [11], pancake-chamber engine [27,28] or square piston engine [29]. These studies can mainly be seen as first steps towards LES of IC engines, but they have already highlighted the capacity of LES to accurately resolve in-cylinder flow structures. Concerning cycle-to-cycle variations, the works reported in [22,30–32] are probably the most interesting ones. They describe multiple engine cycle simulations in an axisymmetric piston-cylinder assembly with a fixed central valve. Although this configuration is not totally representative of real engine functioning (no combustion, missing intake and exhaust ducts) results clearly demonstrate that LES has the inherent potential to capture cycle-to-cycle variations.

A second category of studies is devoted to more realistic configurations. In many cases, only one cycle (complete or partial) is reported [33–38] and no conclusion concerning cyclic variability can be drawn. In [39], a multi-cycle simulation of a Diesel engine with intake and exhaust manifolds is presented. Nevertheless the conclusions drawn regarding the potential of LES to capture cyclic variability are questionable since only two cycles are compared, the first one being much dependent of the initial conditions. Haworth [22] simulates four cycles of a two-valve four-stroke engine without combustion. The temporal evolution of in-cylinder swirl and tumble ratios clearly exhibits cycle-to-cycle variations but no explanation is given as to their causes. Dugué et al. [40] attempts to reproduce with LES the cyclic variability observed experimentally in a four-valve Diesel engine. The ten computed cycles highlight cycle-to-cycle variations but only from an aerodynamic point-of-view since the combustion

is not accounted for. Goryntsev et al. [41] study the impact of cycle-to-cycle velocity fluctuations on fuel spray injection and mixing processes in a realistic direct fuel injection engine. Results highlight the occurrence of cycle-to-cycle mixture variations at the spark plug location but the consequences on the combustion phase are not discussed. Adomeit et al. [42] present a study of interactions between the intake flow and fuel injection in a direct injection SI engine using LES with a commercial CFD code. The simulation of ten independent cycles from intake valve opening up to just before spark ignition, combined with a statistical treatment of the results, allows to illustrate how small variations in initial conditions can lead to important variations of the conditions at the spark plug, and thus cyclic variations. Although the presented approach allows to qualitatively evaluate the propensity of the studied engine to exhibit cycle-to-cycle variations, the authors conclude that LES of a number of consecutive complete engine cycles comprising in particular the full combustion phase would be necessary to yield a more quantitative assessment.

Most CFD codes used in the cited studies are based on numerical schemes originally dedicated to RANS, often privileging stability over precision. Second-order upwind schemes are often used for convection terms despite their very dissipative nature which may affect the energy spectrum at high wave numbers [22,43]. For time integration, first-order implicit schemes are commonly used. As pointed out by Dugué et al. [40] the usage of such methods with excessive CFL numbers to limit the necessary computational time, considerably decreases the convective scheme precision and as a consequence the quality of the LES. As a solution, the authors propose to limit the acoustic CFL number, keeping it close to unity as much as possible.

In summary, very few LES studies deal with cycle-to-cycle combustion variations in realistic piston engine configurations using a CFD code tailored for LES. Recently, a first study on SI engine combustion using a dedicated LES code as well as a specifically developed LES model for premixed spark ignited combustion has been published [44]. The present work constitutes the following step: its objective is to explore the potential LES has to reproduce the occurrence of cyclic variability, and to help identify their causes.

A priori there are two strategies to reach this objective: the perturbed single-cycle approach or the multi-cycle approach. The perturbed single-cycle approach consists in performing several single-cycle, independent LES. For each cycle, a perturbation is introduced on a chosen variable. The sensitivity and the reaction of the engine to the perturbation as well as its stable or unstable behavior may then be analyzed. In contrast the multi-cycle approach requires only one LES, but which covers a time span long enough to include a sufficient number of engine cycles to yield statistically relevant results. The results can then be processed as would be those acquired experimentally on a real engine. At first sight the single-cycle approach is attractive because the independent simulations can be run in parallel, limiting computational time to yield a statistical result. Moreover, depending on the objectives of the study, only a part of the engine cycle is generally calculated: whereas the intake and/or combustion strokes are most of the time included, the exhaust stroke is often neglected to reduce computational costs. However the results obtained with this method will largely depend on the perturbations introduced into the individual LES. Many choices are in principle possible in terms of perturbed variable (pressure, temperature, mean velocity, turbulent intensity, etc), type of condition to perturb (initial condition or boundary condition) and amplitude (and phase) of the perturbations. In the absence of objective information

resulting e.g. from experiments on reasonable perturbation amplitudes, this approach can thus only allow a qualitative study of the propensity of an engine to generate variations, but with no quantification of their importance and full impact.

In contrast, the main drawback of the multi-cycle approach is the important computational time needed to cover a sufficiently large number of engine cycles required to yield converged statistical quantities. Furthermore, the dependency on the initial conditions remains problematic and may increase the number of cycles required. Indeed, and although suggested by different authors [22,40], it is not clear whether one cycle is enough to achieve results independent of the initial fields. Nevertheless, the multi-cycle approach presents a major advantage: if all physical phenomena influencing flow and combustion in the engine are accurately accounted for, it should yield a direct quantitative view at cyclic variations and their effects. Moreover, from a physical point of view, it is surely the most convincing method to reproduce real engine operation where each individual cycle depends of the in-cylinder conditions at the end of the previous one. Finally, this is probably the only way to account for acoustic effects in the intake and exhaust ducts, which may be essential at high and full loads.

In the present work, we chose to explore the multi-cycle approach, and in particular the predictions one can expect for a realistic number of computed cycles. The simulation is performed using a Large-Eddy simulation technique with a solver specifically dedicated to LES and its requirements (Section 2). The combustion is modeled with a Coherent Flame Model (CFM) (Section 3), combined with a spark ignition model that is particularly suited for piston engine applications. The considered geometry is a single cylinder XU10 SI en-

gine fuelled with a gaseous propane-air mixture (Section 4) whose variability was previously observed experimentally [45]. The simulation time of the LES covers ten complete four-stroke engine cycles. Numerical results highlight the capacity of LES to reproduce realistic cycle-to-cycle variations (Section 5). They also illustrate how LES can bring a new insight into the causes and mechanisms of cyclic variability.

2 Numerical approach

LES solver

The AVBP LES solver is a fully explicit 3D CFD code solving the unsteady, compressible, multi-species Navier-Stokes equations on unstructured and hybrid grids. It is based on a cell-vertex finite-volume approximation [46,47]. In this work space and time discretization are performed using an explicit second-order Lax-Wendroff scheme [48]. This centered scheme allows to describe the resolved scales of the flow without excessive dissipation, as required by LES. Moreover, its computational cost is rather low.

The subgrid stress tensor in the momentum equation is modeled using a Smagorinsky model [49] with a constant coefficient $C_s = 0.18$. Combustion is described by the ECFM-LES model coupled with the AKTIM-based spark ignition model, both being detailed in Section 3. Flame/wall interactions are taken into account extending the model of Bruneaux et al. [50] to LES.

The boundary condition treatment is based on a multi-species extension [47] of the Navier-Stokes Characteristic Boundary Conditions (NSCBC) [51] which ensure a physical representation of acoustic waves propagation at boundaries. Finally the mesh management is handled by an Arbitrary Lagrangian Eulerian method [52] combined with a Conditioned Temporal Interpolation technique [11] originally developed for RANS computations [53].

Parallelism

AVBP is a code dedicated to massively parallel computations. Its architecture based on the MPI library is specifically built to allow an optimum efficiency up to several thousands processors [17,18,54]. For the present computation,

the return time for one full LES cycle was 120 hours on 32 Xeon processors of a Linux cluster with an ethernet network.

3 Premixed combustion modeling

Premixed combustion processes are usually characterized by the Damköhler and the Karlovitz numbers respectively noted Da and Ka , and defined as:

$$Da = \frac{\tau_t}{\tau_c} \quad (1)$$

$$Ka = \frac{\tau_c}{\tau_k} \quad (2)$$

where τ_t is the integral time scale, τ_k the Kolmogorov time scale and τ_c the chemical time scale estimated from the laminar premixed flame speed and thickness. For piston engines these non-dimensional numbers can be roughly evaluated: $10 < Da < 100$ and $0.01 < Ka < 1$ [44]. In terms of length and velocity scales and for a turbulent flow characterized by an integral length scale l_t and a large-scale velocity fluctuation u' , this corresponds approximately to $10 < l_t/\delta_l < 100$ and $1 < u'/S_l < 10$ where δ_l is the flame thickness and S_l is the flame speed. Following Peters' combustion diagram [55] reproduced in Fig. 1, combustion in spark ignition engines thus mainly occurs in the flamelet regime. In this regime, chemical reactions take place in very thin regions whose structure is similar to a laminar flame. The flame front may then be considered as a collection of wrinkled interfaces separating cold unburned reactants from hot burned products.

Among the combustion models developed for the flamelet regime, the Coherent Flame Model (CFM) is particularly suited for piston engine applications. This model is based on the use of a transport equation for the flame surface

per unit volume or Flame Surface Density (FSD). It has been widely used in the automotive industry for RANS calculations [53,56]. In the frame of SI engine applications, the CFM approach presents a significant advantage compared to classical algebraic models like the model of Boger [57] as it allows to handle non-equilibrium situations between flame surface production and destruction. This is of main importance in piston engines where the flame wrinkling increases during combustion and therefore can not be supposed in equilibrium [44]. The following Section presents a recent extension to LES of this model, the ECFM-LES model used in this study. Then, the spark ignition model is described in Section 3.2.

3.1 The ECFM-LES combustion model

The ECFM-LES model constitutes a synthesis of RANS and LES developments:

- the ECFM model [53,56] is a RANS model that extended the original CFM model [58] to partially premixed mixtures and variable unburned gases temperature. This extension is based on a conditioning technique which allows precise reconstruction of local properties in fresh and burned gases even in the case of high levels of local stratification;
- the CFM-LES model [44] is an adaptation of the original CFM model to LES. The FSD transport equation is based on a spatial filtering adapted to LES, accounting for the effects of the resolved flow on the flame surface. First encouraging results relating to piston engine applications are reported in [44]. In particular, it has been shown that the total reaction rate is almost independent of the mesh resolution, which is an essential feature for

LES modeling, only the ratio between resolved and unresolved contributions varies.

The ECFM-LES model combines these two approaches: the formalism of the CFM-LES model is extended to non homogeneous mixture properties as proposed in the ECFM model. In the following parts, the main features of ECFM-LES are presented. For a complete description of the conditioning technique and of the LES FSD equation, the reader should refer to [56,59] and [44] respectively.

3.1.1 LES combustion filter size

In SI engines the typical flame thickness for stoichiometric premixed flames is about 0.1 mm [2], i.e. smaller than mesh resolutions in current use ($\Delta_x \approx 0.5 \text{ mm}$). Moreover with the finite volume approach used in this study (and in most CFD codes) a minimum of 5 to 10 grid points is generally required to describe the flame front. Consequently, the reacting zone cannot directly be resolved on the computational mesh using a classical LES filter of size Δ_x . In practice, a LES combustion filter of size $\hat{\Delta} = n_{res}\Delta_x$ is used, where n_{res} is a resolution parameter such that $5 < n_{res} < 10$. The flame brush thickness is then close to $\hat{\Delta}$. Hence, all the equations presented below are filtered at scale $\hat{\Delta}$. To avoid modifying the mixing processes involved in the energy and species transport equations outside of the flame front, a dynamic procedure is adopted: the LES combustion filter is only used inside the reaction zone and the classical filter Δ_x is applied elsewhere.

3.1.2 Species and energy transport equations

In the ECFM formalism, the mixture composition is computed solving transport equations for the filtered mass densities $\bar{\rho}_i = \bar{\rho}\tilde{Y}_i$ of chemical species [56]. For the present calculations, only major species are considered: O_2 , N_2 , CO_2 , H_2O , CO and H_2 .

$$\frac{\partial \bar{\rho}\tilde{Y}_i}{\partial t} = -\nabla \cdot (\bar{\rho}\tilde{\mathbf{u}}\tilde{Y}_i) + \nabla \cdot \left(\sigma_c \bar{\rho} \left(\frac{\nu}{Sc} + \frac{\hat{\nu}_t}{Sc_t} \right) \nabla \tilde{Y}_i \right) + \bar{\rho}\tilde{\dot{\omega}}_i \quad (3)$$

In the above equation, terms of the type \bar{Q} denote filtered quantities (Reynolds filter) and terms of the type \tilde{Q} , mass weighted filtered quantity (Favre filter), both filtered quantities being linked by the relation: $\bar{\rho}\tilde{Q} = \overline{\rho Q}$. $\bar{\rho}$ is the mean density and $\tilde{\mathbf{u}}$ the Favre filtered velocity vector. ν is the molecular kinematic viscosity and $\hat{\nu}_t$ the turbulent kinematic viscosity estimated at scale $\hat{\Delta}$:

$$\hat{\nu}_t = C\hat{u}'\hat{\Delta} \quad (4)$$

As a first approach, \hat{u}' is estimated from the subgrid scale (sgs) turbulence intensity u' assuming a Kolmogorov cascade:

$$\hat{u}' = u' \left(\hat{\Delta} / \Delta_x \right)^{1/3} \quad (5)$$

where u' is obtained from the Smagorinsky model by a simple dimensional relation:

$$u' = \nu_t / C\Delta_x \quad (6)$$

with $C = 0.12$. Sc and Sc_t in Eq. 3 denote the molecular and turbulent Prandtl numbers. Based on an analytical expression of the flame brush thickness, Richard et al. [44] proposed an algebraic expression for the factor σ_c which mainly depends on the flame front resolution parameter n_{res} defined by

the user. As shown in the validation case below, the factor σ_c allows to impose a flame brush thickness approximately equal to $\hat{\Delta} = n_{res}\Delta_x$.

The fuel density is decomposed into unburned and burned parts:

$$\bar{\rho}_F = \bar{\rho}_F^u + \bar{\rho}_F^b \quad (7)$$

Transport equations similar to that of other species are defined for these fuel densities $\bar{\rho}_F^x = \bar{\rho}\tilde{Y}_F^x$, where the superscript x represents either the unburned part “u” or burned part “b”:

$$\frac{\partial \bar{\rho}\tilde{Y}_F^x}{\partial t} = -\nabla \cdot (\bar{\rho}\tilde{\mathbf{u}}\tilde{Y}_F^x) + \nabla \cdot \left(\sigma_c \bar{\rho} \left(\frac{\nu}{Sc} + \frac{\hat{\nu}_t}{Sc_t} \right) \nabla \tilde{Y}_F^x \right) + \bar{\rho}\tilde{\omega}_F^x \quad (8)$$

Finally, a transport equation for the mean sensible enthalpy \tilde{h}_s is solved:

$$\frac{\partial \bar{\rho}\tilde{h}_s}{\partial t} = -\nabla \cdot (\bar{\rho}\tilde{\mathbf{u}}\tilde{h}_s) + \nabla \cdot \left(\sigma_c \left(\frac{\lambda}{Pr} + \frac{\hat{\lambda}_t}{Pr_t} \right) \nabla \tilde{h}_s \right) + \bar{\rho}\tilde{\omega}_{h_s} \quad (9)$$

where λ and $\hat{\lambda}_t$ are the molecular and turbulent conductivities and Pr and Pr_t the molecular and turbulent Prandtl numbers. As diffusivities in species and energy equations need to be equal in the CFM approach, $Pr = Sc$ and $Pr_t = Sc_t$.

3.1.3 Unburned and burned gases properties

In the CFM approach, the flame thickness is supposed infinitely small, then the gases can be present only in two possible states: unburned and burned. In order to define correctly the species mass fractions in the unburned state for variable equivalence ratio and dilution flows, transport equations for the species tracers \tilde{Y}_{Ti} are introduced [53,56]. These transport equations are identical to the mean

species transport equations (Eq. 3) except that the reaction source term due to combustion is not included. For the fuel, a similar tracer \tilde{Y}_{TF} is transported. We assume that unburned gases can contain any of seven species defined precisely: Fuel, O_2 , N_2 , CO_2 , H_2O , H_2 and CO . As four atomic elements are present (O, C, H, N), four atomic mass balance equations can be written. In consequence, only three tracer species equations are required.

\tilde{Y}_{Ti} represents the species mass fraction conditioned in the fresh gases $\tilde{Y}_i|^u$ [53,56]:

$$\tilde{Y}_{Ti} = \tilde{Y}_i|^u = \bar{\rho}_i^u / \bar{\rho}^u \quad (10)$$

where $\bar{\rho}_i^u$ is the mass of species (or fuel) present in the fresh gases per unit volume and $\bar{\rho}^u$ is the mass of fresh gases per unit volume.

Unburned, burned and mean densities are of course related as follows:

$$\bar{\rho}_i = \bar{\rho}_i^u + \bar{\rho}_i^b \quad (11)$$

$$\bar{\rho} = \bar{\rho}^u + \bar{\rho}^b \quad (12)$$

These tracer species equations allow to define completely the unburned gases composition $\tilde{Y}_i|^u$.

The mass filtered progress variable \tilde{c} can now be defined, as in the ECFM-RANS model [56], as the burned gases mass fraction: $\bar{\rho}^b = \tilde{c}\bar{\rho}$. This relation is equivalent to $\bar{\rho}^u = (1 - \tilde{c})\bar{\rho}$ (using Eq. 12). Assuming that all species present in the unburned gases cross the flame interface at the same volumetric flow rate, \tilde{c} is defined in practice using the unburned and tracer fuel mass fractions:

$$\tilde{c} = 1 - \frac{\tilde{Y}_F^u}{\tilde{Y}_{TF}} \quad (13)$$

Introducing these relations into Eq. 11 the relationship between unburned, burned and mean mass fractions can be deduced:

$$\tilde{Y}_i = (1 - \tilde{c})\tilde{Y}_i|^u + \tilde{c}\tilde{Y}_i|^b \quad (14)$$

Equation 14 allows to define completely the conditional burned gases composition $\tilde{Y}_i|^b$.

In piston engines, the unburned gases temperature T^u evolves during the compression and expansion strokes due to the variation of pressure, and also due to the equivalence ratio and dilution stratification when fuel and air are not perfectly premixed. For this reason, a transport equation for the unburned gases enthalpy \tilde{h}_s^u was introduced by Duclos and Zolver [53]. Knowing \tilde{h}_s^u and $\tilde{Y}_i|^u$ allows to compute T^u . Relation 14 is also true for any massic quantity, consequently, the burned gases enthalpy can be deduced from:

$$\tilde{h}_s = (1 - \tilde{c})\tilde{h}_s^u + \tilde{c}\tilde{h}_s^b \quad (15)$$

Again, knowing \tilde{h}_s^b and $\tilde{Y}_i|^b$ allows to compute T^b . Finally, the conditional densities in unburned and burned mixtures can be computed:

$$\bar{\rho}|^u = \frac{\bar{p}W^u}{RT^u} \quad (16)$$

$$\bar{\rho}|^b = \frac{\bar{p}W^b}{RT^b} \quad (17)$$

where W^u and W^b are the unburned and burned gases mean molar mass, \bar{p} the mean pressure and R the universal gas constant.

3.1.4 Reaction rate definition

The terms $\tilde{\omega}_i$, $\tilde{\omega}_F^u$ and $\tilde{\omega}_{h_s}$ appearing in the species, unburned fuel and sensible enthalpy transport equations represent the mean reaction rate of the premixed turbulent flame. In the FSD approach it is modeled as:

$$\bar{\rho}\tilde{\omega}_i = \bar{\rho}|^u \tilde{Y}_{Ti} S_l \bar{\Sigma} \quad (18)$$

$$\bar{\rho}\tilde{\omega}_{h_s} = \sum_i h_i^0 \bar{\rho}\tilde{\omega}_i \quad (19)$$

The laminar flame speed $S_l(\bar{\phi}, X_{EGR})$ is computed using a correlation based on the Metghalchi and Keck experiments [60] and taking into account the local fuel/air equivalence ratio $\bar{\phi}$ and the volume fraction X_{EGR} of exhaust-gas recirculation (EGR) [56]. Both $\bar{\phi}$ and X_{EGR} are computed from the unburned gases composition defined previously. Expression 18 simply states that the mean reaction rate is the product of the laminar flame consumption rate per unit surface $\bar{\rho}|^u \tilde{Y}_{Ti} S_l$ times the filtered flame surface density $\bar{\Sigma}$. As discussed in the introduction, $\bar{\Sigma}$ can be estimated alternatively by an algebraic expression or a transport equation. This second choice is retained here.

The reaction rate term in the burned gases mass fraction equation $\tilde{\omega}_F^b$, represents the post-oxydation reactions in the burned gases. As in the present calculations, the fuel/air mixture is nearly homogeneous and lean, these reactions are omitted. Here the same is true for other species present in the burned gases.

3.1.5 Flame Surface Density transport equation

The filtered flame surface density $\bar{\Sigma}$ is determined via the transport equation proposed by Richard et al. [44] in the context of LES:

$$\begin{aligned} \frac{\partial \bar{\Sigma}}{\partial t} = & \underbrace{-\nabla \cdot (\tilde{\mathbf{u}}\bar{\Sigma})}_{T_{res}} + \underbrace{\nabla \cdot \left(\sigma_c \left(\frac{\hat{\nu}}{Sc} + \frac{\hat{\nu}_t}{Sc_t} \right) \nabla \bar{\Sigma} \right)}_{T_{sgs}} \\ & + \underbrace{(\nabla \cdot \tilde{\mathbf{u}} - \mathbf{NN} : \nabla \tilde{\mathbf{u}}) \bar{\Sigma}}_{S_{res}} + \underbrace{\Gamma \left(\frac{\hat{u}'}{S_l}, \frac{\hat{\Delta}}{\delta_l} \right) \frac{\hat{u}'}{\bar{\Delta}} \bar{\Sigma} / \sigma_c}_{S_{sgs}} \end{aligned}$$

$$-\underbrace{\nabla \cdot (S_d \mathbf{N} \bar{\Sigma})}_P + \underbrace{S_d (\nabla \cdot \mathbf{N}) \bar{\Sigma}}_{C_{res}} + \underbrace{\beta S_l \frac{c^* - \bar{c}}{\bar{c}(1 - \bar{c})} (\bar{\Sigma} - \bar{\Sigma}_{lam}) \bar{\Sigma}}_{C_{sgs}} \quad (20)$$

where T_{res} , S_{res} , C_{res} and P are respectively the transport, strain rate, curvature and propagation terms due to resolved flow motions, and T_{sgs} , S_{sgs} and C_{sgs} are respectively the unresolved transport, strain rate and curvature terms. These various contributions are detailed below.

- The propagation term P and resolved curvature term C_{res} ensure the laminar flame propagation when the sgs turbulence is low. They are based on the normal \mathbf{N} to the iso-surface of the filtered progress variable \bar{c} :

$$\mathbf{N} = -\nabla \bar{c} / |\nabla \bar{c}| \quad (21)$$

S_d is the propagation speed relative to the mean flow field of the iso-c surface, defined by:

$$S_d = -(1 + \tau \bar{c}) S_l \quad (22)$$

where $\tau = (\bar{\rho}^u) / (\bar{\rho}^b) - 1$ is the thermal expansion rate across the flame front.

- The sgs curvature term C_{sgs} represents the influence of the unresolved curvature on the flame front wrinkling. To compute this term, the Reynolds filtered progress variable \bar{c} is estimated from the classical BML expression [61,62]:

$$\bar{c} = \tilde{c} \frac{\bar{\rho}}{\bar{\rho}^b} \quad (23)$$

$\beta = 4/3$ and $c^* = 0.5$ are modeling constants and $\bar{\Sigma}_{lam}$ is the laminar part of the FSD defined by (see Richard et al. [44] for the derivation of this expression) :

$$\bar{\Sigma}_{lam} = |\nabla \bar{c}| + (\bar{c} - \tilde{c}) \nabla \cdot \mathbf{N} \quad (24)$$

- The resolved strain S_{res} corresponds to the flame strain rate due to resolved eddies, whereas the sgs strain S_{sgs} accounts for the influence of unresolved structures. As the flame front is filtered at scale $\hat{\Delta}$, all eddies smaller than $\hat{\Delta}$ must be taken into account in the sgs strain [63]. For this purpose, the efficiency function Γ [64] is computed using the turbulent velocity fluctuation \hat{u}' at scale $\hat{\Delta}$. Note that S_{sgs} is modeled inversely proportional to the flame thickness control factor σ_c . In practical engine applications, this term remains of the order of unity, and is therefore of minor influence on the FSD growth rate.
- The unresolved transport term T_{sgs} is classically closed under a gradient assumption and is written as a turbulent diffusion at scale $\hat{\Delta}$.

3.2 The Eulerian AKTIM Spark Ignition model

In SI engines, combustion is initiated by an electrical spark generated by a spark plug. A simple way to model this phenomenon is to impose, at the ignition time t_{ign} , an initial profile of $\bar{\Sigma}$ close to the spark plug. However, the initial sphere of burned gases produced by the electrical discharge has typically a diameter of the order of the inter-electrode distance, i.e. 1 mm. This burned gases volume is naturally filtered on the LES mesh which characteristic cell size is also of the order of 1 mm. Consequently, the initial burned gases volume is filtered on a few cells which leads to a maximal burned gases mass fraction \tilde{c} much smaller than unity. In this situation the ECFM-LES model is not able to correctly describe the global reaction rate because this model assumes the existence of fully burned gases behind the flame front where $\tilde{c} = 1$. It is therefore necessary to control the total reaction rate as long as

the volume occupied by the burned gases is too small to be resolved. The spark ignition model retained in this work is based on this idea. The basic physical equations and assumptions are directly taken from the AKTIM (Arc and Kernel Tracking Ignition Model) model developed in a RANS context [65]. In AKTIM, an ensemble of flame kernels are followed using Lagrangian tracers in order to represent the statistical mean ignition relevant for RANS. Instead, the Eulerian field of the progress variable \tilde{c} is chosen in the present approach to track the initial flame kernel. This choice is in better agreement with the LES hypothesis which induces that the calculated engine cycle is not a statistical mean like in RANS, but a possible realization.

The Eulerian AKTIM model, described in [44], combines three phases:

- First, an initial spherical profile of progress variable is imposed at spark time t_{ign} :

$$\tilde{c}(\mathbf{x}, t_{ign}) = \frac{c_0}{2} \left(1 - \tanh \left(\frac{\mathbf{x} - \mathbf{x}_{spk}}{\delta_{ign}} \right) \right) \quad (25)$$

where δ_{ign} is the mean value of $\hat{\Delta}$ in the vicinity of the spark plug, \mathbf{x}_{spk} is the position of the spark plug electrodes and c_0 is an arbitrary small parameter;

- After time t_{ign} , the reaction rate (or FSD) is estimated from the progress variable using an algebraic expression [57]:

$$\Sigma_{ign}(\mathbf{x}, t) = \alpha \tilde{c}(\mathbf{x}, t) (1 - \tilde{c}(\mathbf{x}, t)) \quad (26)$$

where α is a global coefficient determined by imposing the integral of $\Sigma_{ign}(x, t)$ over the computational domain Ω to be equal to the total surface $S_{tot}(t)$:

$$\alpha = \frac{S_{tot}(t)}{\int_{\Omega} \tilde{c}(\mathbf{x}, t) (1 - \tilde{c}(\mathbf{x}, t)) dV} \quad (27)$$

$S_{tot}(t) = \Xi_{ign}(t) S_{mean}(t)$ is defined assuming that the mean flame kernel surface $S_{mean}(t)$ remains globally spherical and is progressively wrinkled by

turbulence. For this purpose a model equation for the wrinkling coefficient $\Xi_{ign}(t)$ is proposed (see [44] for details).

The algebraic expression of the FSD (Eq. 26) is used until \tilde{c} reaches unity somewhere in the domain, that is, until a complete flame profile has been formed. At this instant $t_{transition}$, the FSD is transferred to the FSD equation (Eq. 20):

$$\bar{\Sigma}(t_{transition}, \mathbf{x}) = \Sigma_{ign}(t_{transition}, \mathbf{x}) \quad (28)$$

- For $t > t_{transition}$, the FSD is given by Eq. 20 and the spark ignition model is not used anymore.

3.3 Academic validations

The behavior of the ECFM-LES combustion model has been evaluated on different academic test cases for which analytical solutions exist. Note that several other tests including validation cases of the spark ignition model have been already reported in [44].

3.3.1 KPP analysis of the ECFM-LES model

The Kolmogorov-Petrovski-Piskunov (KPP) theorem [66–68], based on the assumption of a steady turbulence and of a planar flame propagation in the mean, allows to express the turbulent flame speed as a function of the fresh gases conditions and turbulence. For the proposed ECFM-LES model one can show in an analysis similar to the one performed in [69] and applied to Eq. 20 that:

$$S_{TKPP} = S_l + 2 \left(\sqrt{\frac{C\Gamma}{1 - \frac{\beta c^*}{1+\tau}}} \right) \hat{u}' \quad (29)$$

This theoretical value is then compared to experimental data on turbulent flame speeds for conditions typical of SI engine combustion published by Abdel-Gayed et al. [70]. Figure 2 shows the results obtained for a propane/air mixture at a pressure of 1 *bar* and a temperature of 328 *K*. The turbulent flame speed given by Eq. 29 is shown to be in satisfactory agreement with the measurements for all tested equivalence ratios and turbulence intensities, allowing to verify that the formulation of the ECFM-LES FSD correctly recovers the asymptotic turbulent flame speed for a planar flame propagating into frozen turbulence.

3.3.2 1D laminar and turbulent flame propagation

The first test case is the one-dimensional propagation of a flame in a stoichiometric premixed propane/air mixture. FSD and progress variable profiles are initialized at the center ($x = 0$) of a 1D channel. The inflow velocity of fresh gases is set equal to the KPP speed to stabilize the flame at its initial position. Figure 3 shows that the flame speed S_T converges correctly towards the theoretical value in both laminar and turbulent cases. In the laminar case, the initial Gaussian profile of FSD is simply convected at the laminar flame speed and the convergence is instantaneous. For the turbulent case, the FSD profile takes approximately one characteristic flame time $t_f = \delta_l/S_T$ to reach its steady state value.

The different terms of the FSD transport equation (Eq. 20) are plotted in Fig. 4 for the laminar and turbulent cases. In both cases, the strain rate and curvature due to the resolved flow motion are zero since the configuration is purely one-dimensional. As expected, sgs contributions are also zero in the laminar case where the only non zero contribution is the resolved propagation

term. Finally, the equivalence between FSD, laminar FSD $\bar{\Sigma}_{lam}$ (see Eq. 24), and gradient of the progress variable is well verified in the laminar case. Note that this equality does not hold anymore for the turbulent propagation case where $\bar{\Sigma} > \bar{\Sigma}_{lam}$.

3.3.3 Spherical laminar flame expansion

The behavior of resolved strain rate and curvature terms is checked considering the expansion of a spherical laminar flame. The computational domain is cubic and consists of 64 000 hexahedral elements ($\Delta_x = 0.5 \text{ mm}$). Gaussian profiles of FSD and progress variable are imposed initially. The mixture is stoichiometric and composed of air and propane. For such a configuration, the theoretical flame surface S grows as:

$$S(t) = 4\pi [r_0 + (1 + \tau)S_0 t]^2 \quad (30)$$

where r_0 is the radius of the initial sphere of burned gases. The analytical evolution of the flame surface is compared in Fig. 5 with numerical results obtained with ECFM-LES. After a delay corresponding to the time needed for the initial FSD profile to adapt to the one predicted by the FSD equation, the growth rate predicted by ECFM-LES corresponds to the analytical solution.

3.3.4 Flame propagation on a non-regular mesh

In piston engines the geometry is complex and the meshes can hardly be homogeneous. The purpose of this last test is to check whether the proposed ECFM-LES formulation is able to adapt to non-regular meshes. To this purpose, the planar propagation of a premixed flame is simulated with ECFM-

LES in a rectangular 1D domain comprising two regions with different mesh resolutions, as shown in Fig. 6. The mesh in the central zone has a mesh size twice as large as in the left and right zones. A turbulent flame is initialized at the left side and propagates to the right side in a flow at rest. The factor n_{res} is set to 10 for the computation in order to ensure a resolution of the flame front on a corresponding number of mesh points. The resulting time evolution of the flame speed and thickness are shown in Fig. 7 as the flame propagates through the 1D domain. The flame speed remains constant and independent of the mesh resolution. Only in the transition regions between the mesh zones, a deviation of 20 % can be observed, which vanishes after about one flame time. The thickness of the flame front adapts to the changes in resolution, being twice as large in the coarse mesh region than in the finer one. Figure 8 shows that the flame front remains resolved on 10 grid points as expected, independently of the local mesh resolution.

4 Engine configuration and numerical approach for multi-cycle LES

4.1 Engine parameters and operating point

The studied configuration is a SI single cylinder taken from a production type PSA XU10 engine. As shown in Fig. 9, the geometry employed here includes a flat piston, a cylinder with a pent-roof head and four valves (two for intake on the right of the figure, two for exhaust on the left). A part of the intake and exhaust ducts are also accounted for. The simulated operating point corresponds to a part load case with a volumetric efficiency of 0.35, an engine speed of 2000 revolutions per minute (RPM) and an equivalence ratio

of 0.7. The engine is fuelled with a homogeneous mixture of gaseous propane and air. Table 1 summarizes the main characteristics of the engine and of the chosen operating point.

4.2 *Mesh management*

One of the main difficulties when dealing with piston engine computations is the mesh management. Contrary to body forces methods where the grid stays fixed in spite of the movement of the geometric boundaries [30], ALE techniques consider that each node of a body-fitted mesh moves according to a given speed. Therefore, during the whole engine cycle, the motion of the piston and the valves may induce distortion, contraction or dilatation of the computational meshes. This is problematic for three main reasons:

- in LES, the derivation of the filtered equations is classically based on the assumption that the filtering operator commutes with partial derivatives. This assumption is valid for fixed grids with uniform cell width but commutation errors appear when space-dependent or time-dependent filter widths are considered [71,72]. In piston engine applications, the variations of the cell width imposed by the ALE method may lead to consequent temporal commutation errors. Moureau et al. [73] show that these temporal commutation errors increase with the instantaneous deformation rate of the mesh i.e. with the engine speed and the compression ratio. However, their influence on the computation is found to be negligible for moderate compression ratios (≤ 10) and engine speed (≤ 3000 RPM);
- for hexahedral cells such as the ones used in this study, the aspect ratio of the cells may rapidly increase due to the piston motion since the grid

is stretched or compressed only in one direction, the cylinder axis. The movement of the valves is even more critical because it induces a deformation that is not aligned with the edges of the cells. The problem is that non regular meshes decrease the accuracy of a numerical scheme. For relatively low deformations, it has been shown that the convergence order of the Lax-Wendroff scheme is almost unaffected [47]. But this conclusion is certainly no longer valid for large deformations;

- when the mesh is too compressed, the typical mesh size can reach values far below the spatial scales required by the physics. This situation leads to a waste of computational time since too many elements are then computed. This is all the more true for explicit codes since time steps may then drop excessively.

To use the same grid for the entire computation is not relevant in terms of numerics and computational costs. The solution adopted in this work is to decompose each cycle into several successive mesh phases. Each phase is characterized by a mesh with a constant connectivity, and lasts as long as the deformed mesh keeps a sufficient quality in terms of resolution and numerical accuracy. As soon as this is not the case anymore, the computation is stopped. The obtained solution is interpolated to the mesh of the next phase using a second order interpolation [11,73], and the computation carries on within a new mesh phase. Note that the same set of mesh phases is used for each cycle. In the present computation each engine cycle is split into 20 mesh phases in order to maintain a spatial resolution between 0.2 and 1.5 *mm*. The smallest grid at top dead center (TDC) consists of 254 000 hexahedra, and the largest of 628 000 hexahedra. A typical mesh is shown in Fig. 10. The spark plug is not represented in the mesh but the mesh is refined in the spark plug vicinity

during ignition to gain a finer description of the initial flame kernel. The valve crossover and the first and last 0.5 *mm* of the valve lift are not simulated to avoid too thin cells in the valve seat.

4.3 Initialization and boundary conditions

The simulation starts at intake valve opening (IVO) with flow at rest in the whole geometry. For the thermodynamic initial conditions, three zones are defined: intake ducts, exhaust ducts and cylinder. Pressure and temperature in these three zones are set to the experimental values listed in Table 2. The initial composition in the three zones is assumed to be a perfect mixture of air and propane at the studied equivalence ratio in the intake ducts, and to consist of pure burned gases in the cylinder and the exhaust ducts.

At the intake and exhaust boundaries, mixed inflow/outflow conditions based on the NSCBC method are imposed. Indeed, a simple inflow (respectively outflow) condition can not be set at the intake (respectively exhaust) boundaries because of the back-flow phenomenon that occurs at valve opening. These mixed conditions allow to switch from an inlet formulation to an outlet formulation according to the local and instantaneous direction of the flow. The pressures imposed at intake and exhaust boundaries are time-varying signals extracted from the experimental data. Owing to a lack of cycle-resolved pressure measurements, the same mean signal is repeated for each cycle. As a consequence, acoustic waves in the ducts do certainly not match the experimental behavior, but this is expected to be of minor importance for the present part load case. The temperature and mass fractions imposed at intake and exhaust boundaries are constant and set in accordance with the initial values

in the intake and exhaust ducts (see Table 2). Solid walls are handled using a logarithmic law-of-the-wall formulation for velocity and temperature [21]. Isothermal wall conditions are imposed for the whole geometry with the same wall temperature $T_{wall} = 450 \text{ K}$. In conclusion, it is important to note that no source of cyclic variability is introduced in the computation via the boundary conditions.

4.4 Principle of the multi-cycle simulation

Starting from the initial conditions the LES covers a time span of 7200 crank angle degrees (CAD) and thus comprises ten complete and consecutive four-stroke engine cycles. During the whole simulation the flow in the full geometry is accounted for. In particular the flow in the intake and exhaust ducts is solved for, even when they are closed, to provide proper conditions upon valve opening.

5 Results and discussion

After presenting some main flow features predicted by the LES in Section 5.1, the results of the multi-cycle LES are compared to available experimental data (Section 5.2), before using them to investigate the causes for the observed cycle-to-cycle combustion variations in Section 5.3.

5.1 Main flow features predicted by LES

Description of a typical LES cycle

By convention, each new cycle starts at 355 CAD before combustion TDC when the intake valves open. Just after opening, the intake pressure is lower than the in-cylinder pressure and the burned gases of the preceding cycle flow back out of the cylinder into the intake pipes (not shown). After about 30 CAD, due to the descent of the piston and hence the drop of the in-cylinder pressure, the flow inverts and the fuel/air mixture enters the cylinder. The small lift of the intake valves generates high-speed jets that may locally exceed 250 m.s^{-1} . The interaction between these jets and their impingement on the cylinder walls generate high turbulence levels as well as a large variety of structures. Figures 11 (velocity magnitude) and 12 (equivalence ratio) show the flow during the intake stroke of the third cycle confirming the LES potential to capture a wide range of turbulent scales and structures. This configuration with two intake valves also creates a large scale coherent motion around the y-axis: this so-called tumble motion progressively breaks down during the compression stroke resulting in increased in-cylinder turbulence levels prior to ignition.

Ignition occurs at $t_{ign} = 40$ CAD before combustion TDC. At this crank angle, the fuel/air mixture is almost perfectly mixed with the residual burned gases. The spark ignition model describes the initial kernel growth between t_{ign} and $t_{transition}$ where $t_{transition}$ varies from 21 to 17 CAD before TDC, depending on the considered cycle. Then the ECFM-LES model takes over. The initial spherical kernel (Fig. 13, 1420 CAD) is progressively stretched and wrinkled by the local turbulent flow (Fig. 13, 1430 CAD and 1440 CAD). In contrast

to RANS simulations where all turbulent scales and their effect on the flame front are modelled, the flame front wrinkling by a wide spectrum of turbulent eddies is resolved and clearly visible in LES. The flame reaches first the cylinder head (Fig. 13, 1430 CAD), then the cylinder wall on the exhaust side (Fig. 13, 1450 CAD) and finally blows out on the intake side (Fig. 13, 1470 CAD). The whole combustion process lasts about 130 CAD.

The exhaust stroke starts 143 CAD after combustion TDC. Similarly to the back-flow observed at the beginning of the intake stroke, the flow is first inverted and the fluid in the exhaust pipes tends to enter the combustion chamber (not shown). After about 50 CAD, the “actual” exhaust phase begins and the burned gases are progressively evacuated until valve closure at 355 CAD after combustion TDC. Figure 14 shows a typical temperature field during the exhaust stroke where the cooling effect of the walls may be clearly observed. To conclude with this description of a LES cycle, Fig. 15 allows to go back over an important issue in LES, the subgrid scale viscosity. This figure shows two instantaneous fields of subgrid scale viscosity normalized by the fluid viscosity during the intake and exhaust strokes. This ratio is globally rather low (inferior to 10 in mean), indicating that the mesh resolution seems appropriate in most of the geometry. Of course, these values are very intermittent and highest values (ratio about 100) may be observed locally in space or time, especially at exhaust or intake valve opening when the velocity gradients are very strong in the valve seats. By comparison with RANS computations where this ratio is typically between 100 and 1000, these results confirm the relevance of the present simulation.

Variability of the combustion phase

The time evolution of the flame surface for the simulated cycles is shown in

Fig. 16. In order to ease direct comparisons between the cycles, the time scale for cycles 2 to 10 have been shifted by multiples of 720 CAD to lie in the interval 0 to 720 CAD of the first cycle. Each curve is identified by its cycle number. The resolved part and the total (sgs+resolved) flame surface, both readily available in the ECFM-LES formalism, are displayed. The large contribution of the sgs part in the total flame surface (about 75 – 80%) confirms that the combustion process mainly occurs at subgrid scales. It was shown in [44] that the ECFM-LES model accurately reproduces the changing proportion between resolved and sgs part of combustion as mesh resolution varies, keeping the overall surface constant. Therefore one can state with some level of confidence that despite the important sgs contribution to the flame surface the present results only weakly depend on the mesh resolution. An important level of cyclic variability is observed for both the total and resolved parts and during the whole combustion event. In the following the corresponding variability is compared with experimental findings, before analysing its causes.

5.2 Comparison with experimental findings on cyclic variability

Figure 17 displays the cylinder pressure around combustion TDC for the 10 cycles computed using LES. Experimental mean, minimum and maximum pressure curves are added for direct comparison. Most of the computed cycles lie within the experimental envelop, except the first cycle (marked by a dotted line) that comes out of the envelop during the expansion stroke beyond 30 CAD. This is directly related to the influence of the initial conditions, which leads to a wrong estimation of the trapped mass (see Section 5.3.1). After the second cycle, the influence of the initial conditions does not play anymore a

role, and all pressure curves are superimposed with the experimental curves in the expansion stroke. The large dispersion of the pressure curves indicates a high level of variability. The LES results do not indicate any convergence towards a single pressure curve in relation to an increasing cycle number. This tends to prove that the observed variability is not a long-term effect of the initialization, but a real cycle-to-cycle variation captured by the presented LES. The changes between fast cycles, i.e. those with a maximum cylinder pressure appearing at early crank angles, and slow cycles seem random as a function of the cycle number. The amplitude of these variations is qualitatively in agreement with the measurements, although the simulated cycles tend to remain in the lower part of the experimentally observed envelope.

Another way to highlight cycle-to-cycle variations is to analyze the engine work during the combustion stroke, defined as:

$$W_{comb} = - \int_{V(-\alpha)}^{V(\alpha)} p_{cyl} dV \quad , \quad \text{with } \alpha = 50 \text{ CAD} \quad (31)$$

where p_{cyl} is the cylinder pressure and V the combustion chamber volume. Figure 18 displays the work predicted for the 10 LES cycles along with the values reported experimentally over 300 cycles. According to Pope [14] there is no reason, due to the differences in initial and boundary conditions between the experiment and the LES and the fact that subgrid scale models are derived from statistical arguments, that the 10 simulated cycles correspond to any of the experimental ones. Nevertheless, the LES results are similar to the experimental findings. Table 3 compares the mean work over the 10 simulated cycles and the resulting root mean square (rms) fluctuation around it, with the corresponding experimental findings over 300 cycles. Although the

mean engine work resulting from the few simulated cycles is slightly lower than in the experiment, the level of rms fluctuation of the engine work is quite well reproduced. Even if more cycles would need to be simulated to ascertain that the LES findings are statistically representative, one can conclude that a qualitatively and quantitatively satisfactory reproduction of the observed variability is obtained with the presented simulations.

Figure 19 presents the time evolution during the combustion phase of the volume averaged mean fuel mass fraction in the cylinder. Shown is also the evolution deduced in the experiments from the ensemble averaged mean cycle. Discarding the first LES cycle which is polluted by the initial conditions, all simulated cycles predict the same fuel mass fraction before combustion, slightly underestimated compared to the experimental mean. During the combustion phase, the slope of the fuel mass fraction curves shows values similar to the experimental mean cycle. Also apparent is a large dispersion of LES results, revealing a large cyclic variation of combustion intensities. Finally all the fuel is always entirely consumed.

5.3 Analysis of the origins of cycle-to-cycle variations

The presented multi-cycle LES allows to analyse the causes of the observed combustion variability. In the presented LES no variability has been introduced in the spark ignition model: spark discharge characteristics such as the spark timing, spark duration and spark energy were set identical for all cycles. Following Ozdor [1], and as discussed in Section 1, two main categories of causes remain thus to be considered: mixture-related factors and in-cylinder motion-related factors. In the following both these factors are explored by

post-processing the LES results.

5.3.1 *Mixture-related factors*

A first-order factor for cyclic combustion variability could be cyclic variations of the mixture mass trapped in the cylinder during the combustion phase. In this case the chemical energy that could be released by combustion could vary from cycle to cycle. As shown in Fig. 17 the cylinder pressure curves observed in the experiment, as well as the ones resulting from LES (except for the first cycle influenced by the initial conditions) exhibit a negligible variability during the expansion stroke, which is usually a sign that the trapped mass in all cycles is the same. This is confirmed in Fig. 20 where the total mixture mass trapped in the cylinder during combustion is plotted for the 10 LES cycles. Also shown is the decomposition of the total mass into the mass of the fresh propane/air mixture that entered the cylinder during intake, and the mass of burned residual gases trapped in the cylinder from the preceding cycle. The first LES cycle starts with a residual mass and temperature estimated from experiments and with flow at rest in the cylinder, which is not the case for the ensuing cycles. The influence of these initial conditions can be seen to become negligible after the second cycle, and all ensuing cycles exhibit only a marginal variation of the trapped mass and its composition in terms of fresh and residual gases, which cannot explain the observed variability in terms of cylinder pressure.

A second order factor could be local variations of the composition of the fresh gases mixture. This could lead to local variations of equivalence ratio or dilution by burned gases, thus potentially affecting spark ignition and flame propagation in a different way for each cycle. Figure 21 presents the time

evolution during the combustion phase of the flame surface averaged fuel/air equivalence ratio $\langle\phi\rangle_\Sigma$ obtained by post-processing the LES results. For any quantity Q , $\langle Q\rangle_\Sigma$ is computed as:

$$\langle Q\rangle_\Sigma = \frac{\int_\Omega Q \bar{\Sigma} dV}{\int_\Omega \bar{\Sigma} dV} \quad (32)$$

where Ω is the computational domain. Hence the time evolution of $\langle\phi\rangle_\Sigma$ represents the mean equivalence ratio seen by the flame during its propagation. Although a level of variability is apparent within each cycle, as well as between different cycles, the observed variation amplitude represents only about 0.6% of the overall equivalence ratio for any cycle. Post-processing 3D fields of local mixture composition (not shown here) confirms that local fresh gases composition does only very weakly vary throughout the computational domain during the combustion phase and in different cycles. These variations are thus not sufficient to explain the observed strong cycle-to-cycle combustion variations. Consequently, in the present case, cyclic combustion variability cannot be linked to mixture-related factors.

5.3.2 *In-cylinder motion-related factors*

The nature and characteristics of the in-cylinder flow generated during the intake phase, and its evolution during the ensuing compression and combustion phases, are an essential factor influencing spark ignition and combustion development in piston engines. Two large scale flow patterns are classically distinguished to characterize the nature of the intake flow: swirl, a rotational flow around the axis of motion of the piston (in the present case the z-axis), and tumble, corresponding to a rotation around an axis perpendicular to the latter (i.e. situated in the present x,y-plane). In the present case, the geometry

of the intake favors a tumble motion around the y-axis. In order to quantify the intensity of this flow, the tumble ratio is computed as:

$$T_y = \frac{H}{2\pi M\omega_e} \quad (33)$$

where H is the angular flow momentum around the y-axis, M the moment of inertia around the y-axis and ω_e the engine rotational speed in revolutions per second. The origin for calculating T_y is the centre of mass of the in-cylinder fluid. Figure 22 shows the time evolution of $-T_y$ for the 10 LES cycles from intake valve closure (IVC) up to combustion TDC. The evolution is similar for all cycles: while the level of tumble slightly increases up to about 75 CAD before TDC, the compression by the piston leads to a strong reduction, a phenomenon known as the tumble breakdown. An important level of cyclic variation of the tumble intensity is clearly apparent right at IVC, denoting important variations in the aerodynamic field generated during intake. To a lesser extend cyclic variations of the breakdown rate can also be observed.

A direct effect of the tumbling motion created during intake is the in-cylinder large flow scale velocity field which can be observed looking at the resolved flow field obtained in LES. Figure 23 shows the resolved flow velocity components at spark timing obtained in the 10 LES cycles in the vicinity of the spark plug. Each value is obtained by spatially averaging the velocity components in a small sphere Ω_{sp} of radius 1.5 mm around the spark plug as:

$$\langle \tilde{u}_i \rangle_{sp} = \frac{\int_{\Omega_{sp}} \tilde{u}_i dV}{\int_{\Omega_{sp}} dV}, \quad i = 1, 3 \quad (34)$$

Although the major velocity component is along the x-direction, resulting from T_y , the other flow components are non-negligible, and all three show important cyclic fluctuations. The resulting flow field at the spark plug is complex and

fluctuating from cycle to cycle, which can be expected to directly influence the reproducibility of spark ignition and thus combustion from cycle to cycle. Note that since the physical presence of the spark plug is not accounted for in the present LES, a number of effects such as local modifications of the velocity field and turbulence around the plug, or heat losses towards the spark plug electrodes cannot be investigated. Still, the AKTIM model used in this work allows to account for convective and stretching effects by large flow scales on the early flame kernel development.

The effect of the large scale velocities is finally illustrated in Fig. 24, which displays flame surface density fields in a x - y -plane located just under the spark plug for cycles 5, 6 and 7. Combustion occurs on the exhaust side of the cylinder, due to the strong x -velocities induced by the tumble. For cycles 6 and 7 the y -velocity component is also high, with the effect that the initial flame kernel is in addition convected in the direction of positive y values. For cycle 5 the y -velocity is in contrast negligible, with the result that the flame stays in the centre of the cylinder.

A second, yet indirect, effect of the tumbling motion created during intake is the generation of small scale vortices by the tumble breakdown during compression [1,2,32]. The effect of these small scale vortices is studied looking at the sgs turbulence intensity. Figure 25 illustrates the correlation between sgs turbulence levels at spark timing and a measure of the tumble breakdown. The former is quantified by the flame surface averaged sgs turbulent velocity $\langle \hat{u}' \rangle_{\Sigma}$, obtained from the LES using Eq. 5 and 32 at spark timing. The latter is represented by the difference ΔT_y^{ign} between the maximum value of the tumble ratio during the compression stroke, and the tumble ratio at spark timing: $\Delta T_y^{ign} = (-T_y^{max}) - (-T_y(t = t_{ign}))$. The turbulence level at spark timing shows an important level of cyclic variations, with values ranging between 0.5

and 0.85 m.s^{-1} depending on the cycle. These variations show a good correlation with the variations of the tumble breakdown, confirming the direct link between both.

This high variability of the turbulent velocity significantly influences the flame development in the early times of combustion. A measure of the duration of this early flame development can be given by the difference $CA_{10} - CA_{ign}$ where CA_{10} is the crank angle at which 10% of the trapped fuel has been consumed, and CA_{ign} is the spark timing in crank angles. Figure 26 displays this quantity versus $\langle \hat{u}' \rangle_{\Sigma} (t = t_{ign})$ for the 10 LES cycles. The important variations of the combustion rate in early times of combustion show a clear correlation with the small-scale turbulence fluctuations in the spark plug vicinity: the cycles burning the fastest correspond to the highest small scale turbulence levels. This ascertains the indirect link between the cyclic variation of the tumble ratio and the rate of combustion just after spark timing, via the tumble breakdown mechanism that generates small scale turbulence around the spark plug.

The conclusions drawn concerning the link between intake aerodynamics and early flame development can be extended to the whole combustion process. Figure 27 shows the correlation between a measure for the overall combustion duration expressed as $CA_{90} - CA_{ign}$ where CA_{90} is the crank angle when 90% of the fuel is consumed, and the overall tumble drop due to breakdown ΔT_y^{TDC} defined as $\Delta T_y^{TDC} = (-T_y^{max}) - (-T_y (t = TDC))$. The link between these two quantities, although simplistic at first sight, is evident: the cycles presenting the highest tumble drop clearly burn the fastest. Note that if the difference in tumble ratio is replaced by the maximum tumble ratio, the obtained correlation is much lower than the one shown for the tumble drop.

In summary it clearly appears from the presented analysis of the 10 simulated LES cycles that the cyclic fluctuations of the tumble motion, and its coupling with spark ignition and combustion, is the main cause for the cycle-to-cycle combustion variations observed experimentally in the cylinder pressure curves. The cyclic variations of tumble ratio have a direct influence via the large scale velocity variations induced, and an indirect effect via the variations in tumble breakdown, which generates variations in the intensity of the small scale velocity field. In the present study the relative importance of the large scale velocity field appears to be lower than the one related to small scale fluctuations.

A number of different factors for such a cyclic variability of the tumble motion can a priori be identified. First, the variations of overall combustion rate lead to small variations in the thermodynamic conditions of the residual gases remaining in the cylinder, which lead to small variations in the in-cylinder conditions upon intake valve opening. Furthermore the turbulent nature of the flow naturally leads to cyclic variations, as its non-linear behavior can amplify slight cyclic differences that would otherwise have a negligible effect. It is worthwhile noting that in the present case the stability of the trapped mass indicates that globally, the intake process reveals negligible variations. The cyclic variations do not affect integral quantities like overall mass flow, but lead to local differences in flow structure that find an important amplification via the tumble breakdown and combustion. The decisive influence of such local and unsteady phenomena on the global engine behavior, unpredictable with RANS approaches, is a good illustration of what LES can bring in engine applications.

6 Conclusion

This paper describes one of the first attempts to perform reactive multi-cycle LES in a real spark ignition engine configuration. The basis for this study was the development of the ECFM-LES model able to reproduce the effects of both the resolved, large scale and the unresolved, subgrid scale motions on spark ignition and propagation of a turbulent flame in the cylinder of a piston engine. Some basic test cases were presented to illustrate the well-posedness of the resulting model for the presented application. It was then used in combination with the AVBP LES flow solver to simulate a time span of 7200 crank angles, thus encompassing 10 consecutive full four-stroke engine cycles in a single cylinder XU10 four-valve geometry fuelled with a pre-mixture of gaseous propane and air. An analysis of the LES findings was then compared with experimental findings on cylinder pressure evolutions, and LES is found to capture both qualitatively and quantitatively the cycle-to-cycle combustion variations observed experimentally. A detailed investigation of the root causes of this cyclic variability revealed that in the present configuration the cyclic variations of the coherent tumble motion generated during the intake, and consequently of the turbulence intensity during ignition combustion, was the main triggering factor. In the studied case, variations in the overall or local mixture were not found of sufficient importance to induce significant modifications in the combustion process.

The conclusions drawn in this study have to be considered with care as only a small number of cycles were computed, and as many LES findings could not be validated due to a lack of adequate experimental data. Nevertheless, this work clearly illustrates why and how LES can be used to study unsteady

phenomena in piston engine applications. In addition to cyclic variations, LES could bring significant improvements compared to classical RANS computations when it comes to understand and even predict unsteady phenomena like misfires, knocking or fast transients between operating points for instance.

However, the validation and the generalization of such LES calculations still require consequent efforts in various directions:

- the lack of experimental data tailored to validate LES is now a major obstacle. Validation of complex phenomena such as intake flow aerodynamics, mixture formation or combustion requires huge cycle-resolved experimental databases that are not available yet. This lack of cycle-resolved information also increases the difficulty to specify unsteady boundary conditions which are of main importance in such calculations. For instance in this work, since the experimental cycle resolved signals were unknown at inlets and outlets, only a phase mean signal was used to impose the pressure at the boundaries;
- SI engines fuelled with a gaseous premixed fuel are of marginal interest for today's engine concepts. Other systems such as in particular direct gasoline injection involve various other phenomena, as the interaction between intake aerodynamics and liquid fuel injection, that could not be studied in the present case. The presented findings would thus surely need to be reconsidered for direct injection engines;
- despite the growing performances of massively parallel machines, the computational cost is still a limiting factor. Although computing ten cycles has been sufficient to extract relevant information and tendencies, this is probably insufficient to draw statistical conclusions in the general case. Heywood [2] suggests that a minimum of 50 engine cycles must be acquired

experimentally to yield statistically reliable results. In the present case the return time for a whole cycle was 120 hours on a 32 Xeon processors Linux cluster. Considering the fast development of computational power, calculating 50 cycles may become possible in the near future, but will also require further improving the capabilities of advanced solvers like the used AVBP code;

- finally, acoustic effects in the intake and exhaust pipes have been deliberately neglected in the present work due to the low load operating condition considered. This assumption does probably not stand anymore at high and full load where acoustic waves in the intake and exhaust ducts can be expected to greatly influence the occurrence and importance of cyclic variability. Here coupling the LES flow solver, able to realize LES of the flow inside the combustion chamber and a part of the intake and exhaust ducts attached to it, with a 1D CFD code, able to simulate the remaining engine under the assumption of planar longitudinal flow, could help to overcome this limitation at reasonable computational cost.

Acknowledgements

This work was partly funded by the European Commission under project number NNE5-2001-00495 'LESSCO2'. We kindly acknowledge the support from Dr. T. Poinsot for fruitful discussions and of the CERFACS CFD Team (Toulouse, France) for providing part of the necessary computational resources.

References

- [1] N. Ozdor, M. Dulger, E. Sher, SAE Paper 950683, 1994.
- [2] J. Heywood, Internal combustion engine fundamentals, McGraw-Hill, New-York, NY, USA, 1988.
- [3] M. B. Young, SAE Paper 810020, 1981.
- [4] M. Rashidi, Comb. Flame 42 (1981) 111–122.
- [5] K. Hamai, H. Kawajiri, T. Ishizuka, M. Nakai, Proc. Combust. Inst. 21 (1986) 505–512.
- [6] P. G. Hill, Comb. Flame 72 (1988) 73–89.
- [7] S. Bates, SAE Paper 892086, 1989.
- [8] R. S. Barlow, Proc. Combust. Inst. 31 (2006) 49–75.
- [9] M. Drake, D. Haworth, Proc. Combust. Inst. 31 (1) (2007) 99–124.
- [10] W. Jones, B. Launder, Int. J. Heat Mass Transfer 15 (1972) 301–314.
- [11] V. Moureau, I. Barton, C. Angelberger, T. Poinsot, SAE Paper 2004-01-1995, 2004.
- [12] R. Rogallo, P. Moin, Ann. Rev. Fluid. Mech. 16 (1984) 99–137.
- [13] C. Meneveau, J. Katz, Ann. Rev. Fluid Mech. 32 (2000) 1–32.
- [14] S. B. Pope, New Journal of Physics 6 (2004) 35.
- [15] M. Lesieur, O. Métais, P. Compte, Large-Eddy Simulations of Turbulence, Cambridge University Press, U.K., 2005.
- [16] F. Ham, S. V. Apte, G. Iaccarino, X. Wu, M. Herrmann, G. Constantinescu, K. Mahesh, P. Moin, in: Annual Research Briefs, Center for Turbulence Research, NASA Ames/Stanford Univ., 2003 pp. 139–160.

- [17] G. Staffelbach, L. Y. M. Gicquel, T. Poinsot, in: *Int. Symp. on Complex Effects in Large Eddy Simulation*, Cyprus, 2005.
- [18] G. Staffelbach, T. Poinsot, in: *Super Computing 2006*, Tampa, FL, USA, 2006.
- [19] C. Martin, L. Benoit, Y. Sommerer, F. Nicoud, T. Poinsot, *AIAA J.* 44 (4) (2006) 741–750.
- [20] L. Selle, L. Benoit, T. Poinsot, F. Nicoud, W. Krebs, *Combust. Flame* 145 (1-2) (2006) 194–205.
- [21] P. Schmitt, T. Poinsot, B. Schuermans, K. Geigle, *J. Fluid Mech.* 570 (2007) 17–46.
- [22] D. Haworth, *Oil and Gas Science Tech.* 54 (2) (1999) 175–185.
- [23] S. El Tahry, D. C. Haworth, *J. Propuls. Power* 8 (1992) 1040–1048.
- [24] I. Celik, I. Yavuz, A. Smirnov, *Int. J. Engine Research* 2 (2) (2001) 119–148.
- [25] L. Thobois, G. Rymer, T. Souleres, *SAE Paper 2004-01-1854*, 2004.
- [26] L. Thobois, G. Rymer, T. Souleres, T. Poinsot, B. Van den Heuvel, *Int. J. Vehicle Des.* 39 (4) (2005) 368–382.
- [27] K. Nishiwaki, Y. Yoshihara, K. Saijyo, *SAE Paper 2000-01-1897*, 2000.
- [28] K. Saijyo, K. Nishiwaki, Y. Yoshihara, *SAE Paper 2003-01-1818*, 2003.
- [29] K. Naitoh, M. Ono, K. Kuwahara, E. Krause, *SAE Paper 2002-01-2694*, 2002.
- [30] R. Verzicco, J. Mohd-Yusof, P. Orlandi, D. Haworth, *AIAA J.* 38 (3) (2000) 427–433.
- [31] D. Haworth, K. Jansen, *Comput. and Fluids* 29 (2000) 493–524.
- [32] M. Fogleman, J. Lumley, D. Rempfer, D. Haworth, *J. Turb.* 5(023).

- [33] A. Smirnov, I. Yavuz, I. Celik, in: ASME Fall Techn. Conf., 99-ICE-247, Ann Arbor, MI, USA, 1999, pp. 119–127.
- [34] K. Sone, S. Menon, in: ASME Tech. Conf., Philadelphia, PA, USA, 2001.
- [35] K. Sone, N. Patel, S. Menon, in: 39th Aerospace Science Meeting, Reno, NV, USA, 2001, Paper AIAA-2001-0635.
- [36] D. Lee, E. Pomraning, C. J. Rutland, SAE Paper 2002-01-2779, 2002.
- [37] B. Hu, C. J. Rutland, SAE Paper 2006-01-0058, 2006.
- [38] K. Naitoh, Y. Kaneko, K. Iwata, SAE Paper 2004-01-3006, 2004.
- [39] R. Jhavar, C. J. Rutland, SAE Paper 2006-01-0871, 2006.
- [40] V. Dugué, N. Gauchet, D. Veynante, SAE Paper 2006-01-1194, 2006.
- [41] D. Goryntsev, M. Klein, A. Sadiki, J. Janicka, in: 5th Symp. on Turb. and Shear Flow Phenomena, Munich, Germany, 2007.
- [42] P. Adomeit, O. Lang, S. Pischinger, R. Aymanns, M. Graf, G. Stapf, SAE Paper 2007-01-1412, 2007.
- [43] R. Mittal, P. Moin, *AIAA J.* 35 (1997) 1415–1417.
- [44] S. Richard, O. Colin, O. Vermorel, C. Angelberger, A. Benkenida, D. Veynante, *Proc. Combust. Inst.* 31 (2) (2007) 3059–3066.
- [45] J.-F. Le Coz, S. Henriot, D. Herrier, J.-J. Marie, P. Barret, in: SIA International Congress, 91012, 1991.
- [46] T. Schönfeld, M. Rudgyard, in: 32nd Aerospace Sciences Meeting & Exhibit, Reno, NV, USA, 1994, Paper AIAA-94-0318.
- [47] V. Moureau, G. Lartigue, Y. Sommerer, C. Angelberger, O. Colin, T. Poinsot, *J. Comput. Phys.* 202 (2) (2005) 710–736.

- [48] P. Lax, B. Wendroff, *Commun. Pure Appl. Math.* 13 (1960) 217–237.
- [49] J. Smagorinsky, *Monthly Weather Review* 91 (1963) 99–164.
- [50] G. Bruneaux, T. Poinso, J. Ferziger, *J. Fluid Mech.* 349 (1997) 191–219.
- [51] T. Poinso, S. Lele, *J. Comput. Phys.* 101 (1) (1992) 104–129.
- [52] C. W. Hirt, A. Amsden, J. L. Cook, *J. of Comp. Phys.* 131 (4) (1974) 371–385.
- [53] J. M. Duclos, M. Zolver, in: *Fourth Int. Symp. on Diagnostics, Modelling of Combustion in Internal Combustion Engines (COMODIA)*, Kyoto, Japan, 1998, pp. 335–340.
- [54] M. Boileau, G. Staffelbach, B. Cuenot, T. Poinso, C. Bérat, in press, *Combust. Flame* (2008), doi:10.1016/j.combustflame.2008.02.006
- [55] N. Peters, *J. Fluid Mech.* 384 (1999) 107 – 132.
- [56] O. Colin, A. Benkenida, C. Angelberger, *Oil and Gas Science Tech.* 58 (1) (2003) 47–62.
- [57] M. Boger, D. Veynante, H. Boughanem, A. Trouvé, *Proc. Combust. Inst.* 27 (1998) 917–927.
- [58] P. Boudier, S. Henriot, T. Poinso, B. T., *Proc. Combust. Inst.* 24 (1992) 503–510.
- [59] O. Colin, A. Benkenida, *Oil and Gas Science Tech.* 59 (6) (2004) 593–609.
- [60] M. Metghalchi, J. Keck, *Combust. Flame* 38 (1980) 143–154.
- [61] K. Bray, M. Champion, P. Libby, *Combust. Sci. Tech.* 55 (1987) 139–161.
- [62] K. Bray, M. Champion, P. Libby, *Proc. Combust. Inst.* 22 (1988) 763–769.
- [63] O. Colin, F. Ducros, D. Veynante, T. Poinso, *Phys. Fluids* 12 (7) (2000) 1843–1863.

- [64] F. Charlette, D. Veynante, C. Meneveau, *Combust. Flame* 131 (2002) 159–180.
- [65] J. M. Duclos, O. Colin, in: *Fifth Int. Symp. on Diagnostics, Modelling of Combustion in Internal Combustion Engines (COMODIA)*, Nagoya, Japan, 2001, pp. 343–350.
- [66] A. N. Kolmogorov, I. G. Petrovski, N. S. Piskunov, *Moscow Univ. Bull. Math., Ser. Int. A* 1 (1937) 1–25.
- [67] N. Hakberg, A. D. Gosman, *Proc. Combust. Inst.* 20 (1984) 225–232.
- [68] F. Fichot, F. Lacas, D. Veynante, S. Candel, *Combust. Sci. Tech.* 89 (1993) 1–26.
- [69] J. Duclos, D. Veynante, T. Poinsot, *Combust. Flame* 95 (1993) 101–117.
- [70] R. Abdel-Gayed, D. Bradley, M. Hamid, M. Lawes, *Proc. Combust. Inst.* 20 (1984) 505–512.
- [71] S. Ghosal, P. Moin, *J. Comput. Phys.* 118 (1) (1995) 24–37.
- [72] S. Leonard, M. Terracol, P. Sagaut, *Comput. Fluids* 36 (2007) 513–519.
- [73] V. Moureau, O. Vasilyev, C. Angelberger, T. Poinsot, in: *Proc. of the Summer Program, Center for Turbulence Research, NASA AMES/Stanford Univ.*, 2004, pp. 157–168

List of Tables

1	Engine specifications and operating point. Crank angle degrees (CAD) are relative to combustion top dead center (TDC).	53
2	Set of LES initial conditions (intake valve opening).	54
3	Mean and fluctuating engine work (Eq. 31): comparison between LES (10 cycles) and experiments (300 cycles).	55

Tables

Bore \times Stroke	8.6 cm \times 8.6 cm
Compression ratio	10
Rotational speed	2000 rpm
Fuel	Propane
Fuel/Air equivalence ratio	0.7
Volumetric efficiency	0.35
Intake valve opening (IVO)	355 CAD before TDC
Intake valve closing (IVC)	143 CAD before TDC
Exhaust valve opening (EVO)	143 CAD after TDC
Exhaust valve closing (EVC)	355 CAD after TDC
Spark timing	40 CAD before TDC

Table 1

Engine specifications and operating point. Crank angle degrees (CAD) are relative to combustion top dead center (TDC).

Zones	Temperature [K]	Pressure [Pa]	Composition	Velocity
Intake ducts	304	0.511×10^5	Fresh gases $\phi = 0.7$	null
Exhaust ducts	813	0.972×10^5	Burned gases	null
Cylinder	813	0.7098×10^5	Burned gases	null

Table 2

Set of LES initial conditions (intake valve opening).

	Mean engine work [J]	Rms engine work [J]
LES	92.68	3.99
Experiments	96.76	3.95

Table 3

Mean and fluctuating engine work (Eq. 31): comparison between LES (10 cycles) and experiments (300 cycles).

List of Figures

- 1 Turbulent combustion diagram proposed by Peters [55]. 60
- 2 Turbulent flame speeds. KPP values: $\phi = 0.7$ — , $\phi = 0.9$, $\phi = 1.1$ --- , $\phi = 1.3$ ——— ; experimental values (Abdel-Gayed et al. [70]): $\phi = 0.7$ \circ , $\phi = 0.9$ \blacksquare , $\phi = 1.1$ \triangle , $\phi = 1.3$ \times . 61
- 3 1D laminar and turbulent flame propagation. Convergence of the computed flame speed towards the theoretical KPP flame speed for the laminar case ($S_{T_{KPP}} = S_l$) (—) and the turbulent case (---). 62
- 4 1D laminar (left) and turbulent (right) flame propagation. Budget of the FSD equation (Eq. 20): diffusion --- ; resolved propagation ——— ; resolved strain rate ---- ; resolved curvature ——— ; sgs strain rate ——— ; sgs curvature Correspondence between FSD (—) and $|\nabla\tilde{c}|$ (\circ) (Eq. 24). 62
- 5 Spherical laminar flame expansion. Theoretical (—) and computed (---) flame surfaces. 63
- 6 Schematic representation of the non-regular mesh. 63
- 7 Propagation on a non-regular mesh. Flame speed $S_T/S_{T_{KPP}}$ — ; flame thickness $\delta_l/\delta_l(t=0)$ ---- . 64

8	Propagation on a non-regular mesh. Flame front resolution at different instants: FSD ($t/t_f = 3.0$ — ; $t/t_f = 8.4$ --- ; $t/t_f = 12.5$) and \tilde{c} profiles ($t/t_f = 3.0$ — \triangle — ; $t/t_f = 8.4$ — \square — ; $t/t_f = 12.5$ — \circ —).	64
9	View of the four-valve SI XU10 engine.	65
10	Computational mesh 70 CAD after intake valve opening.	65
11	Velocity magnitude field at 1225 CAD (cycle 3, 140 CAD after intake valve opening).	66
12	Equivalence ratio field at 1225 CAD (cycle 3, 140 CAD after intake valve opening).	67
13	Iso-surfaces of progress variable ($\tilde{c} = 0.5$) for six increasing times. The crank angle 1440 corresponds to the combustion TDC for the third cycle.	68
14	Temperature field at 1700 CAD (cycle 3, 117 CAD after exhaust valve opening).	69
15	Subgrid scale viscosity normalised by fluid viscosity at 1225 CAD (left) (cycle 3, 140 CAD after intake valve opening) and 1700 CAD (right) (cycle 3, 117 CAD after exhaust valve opening).	69
16	Evolution of total (—) and resolved (.....) flame surface for the ten LES cycles. Curves are numbered according to the cycle they refer to.	70

17	Evolution of cylinder pressure for the ten individual consecutive LES cycles (first cycle: ; nine following cycles: —). Comparison with experimental data: pressure envelope \circ ; phase averaged mean pressure Δ .	70
18	Engine work computed between 50 CAD before TDC and 50 CAD after TDC. Experimental cycles — ; LES cycles \circ .	71
19	Evolution of fuel mass fraction for the ten LES cycles (—). Comparison with experimental mean value (Δ).	71
20	Total trapped mass (\times), fresh gases mass (\circ) and residual gases mass (Δ) in the cylinder for the ten LES cycles.	72
21	Evolution of fuel/air equivalence ratio conditioned on the flame surface $\langle\phi\rangle_{\Sigma}$ for the ten LES cycles.	72
22	Tumble ratio about y-axis during the compression stroke for the ten LES cycles.	73
23	Resolved flow velocity components in the spark plug vicinity at spark timing for the ten LES cycles; x-velocity: + — +; y-velocity: \circ — \circ ; z-velocity: Δ — Δ .	73
24	FSD fields at three instants in cutting planes located just under the spark plug. Exhaust ducts are on the left, intake ducts on the right. Top row: cycle 5; middle row: cycle 6; bottom row: cycle 7. From left to right: 10 CAD before TDC, TDC, 20 CAD after TDC.	74

- 25 Correlation between sgs turbulent velocity at the flame front $\langle \hat{u}' \rangle_{\Sigma}$ and tumble ratio drop at spark timing ΔT_y^{ign} . 75
- 26 Correlation between combustion duration $CA_{10} - CA_{ign}$ and sgs turbulent velocity at the flame front $\langle \hat{u}' \rangle_{\Sigma}$ at spark timing. 75
- 27 Correlation between global combustion duration $CA_{90} - CA_{ign}$ and overall tumble ratio drop ΔT_y^{TDC} during the compression stroke. 76

FIGURES

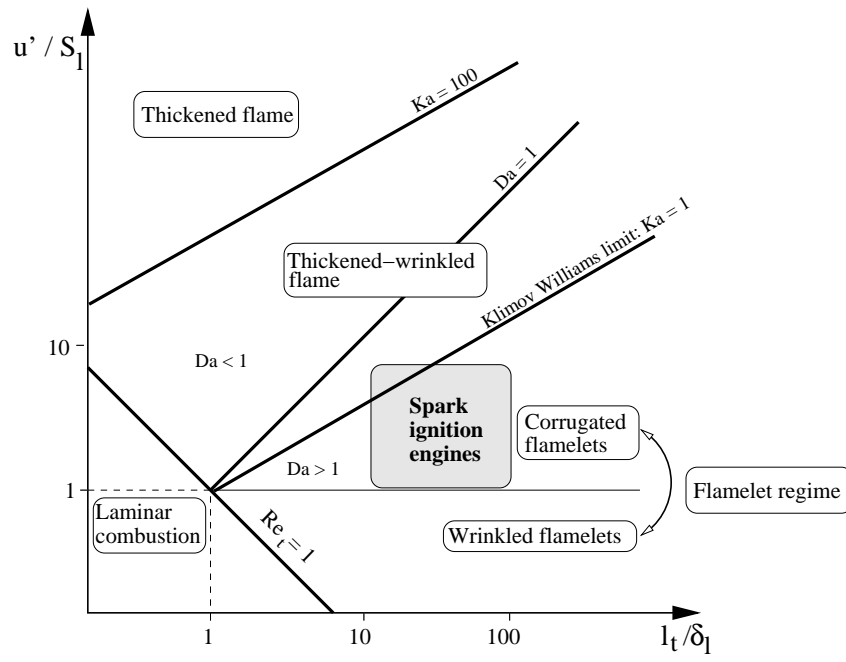


Fig. 1. Turbulent combustion diagram proposed by Peters [55].

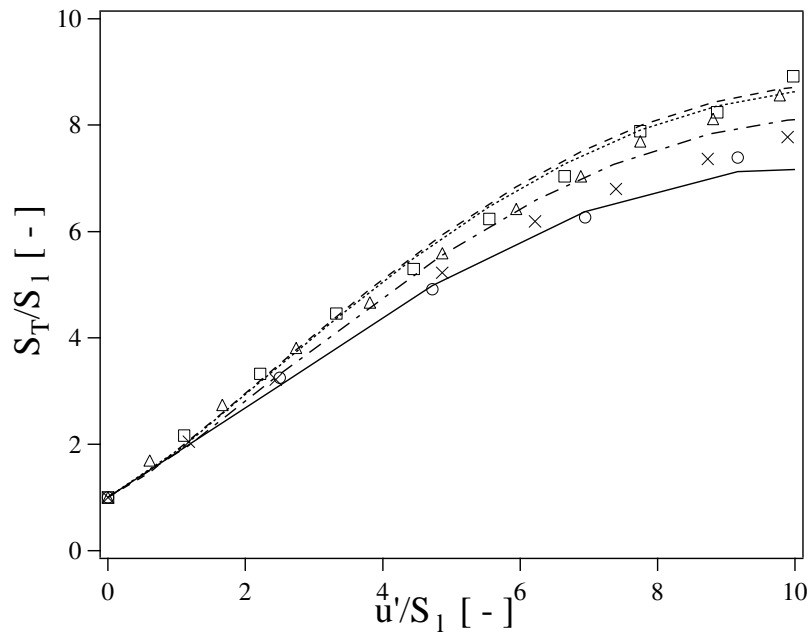


Fig. 2. Turbulent flame speeds. KPP values: $\phi = 0.7$ — , $\phi = 0.9$, $\phi = 1.1$ --- , $\phi = 1.3$ — — ; experimental values (Abdel-Gayed et al. [70]): $\phi = 0.7$ o, $\phi = 0.9$ □, $\phi = 1.1$ △, $\phi = 1.3$ ×.

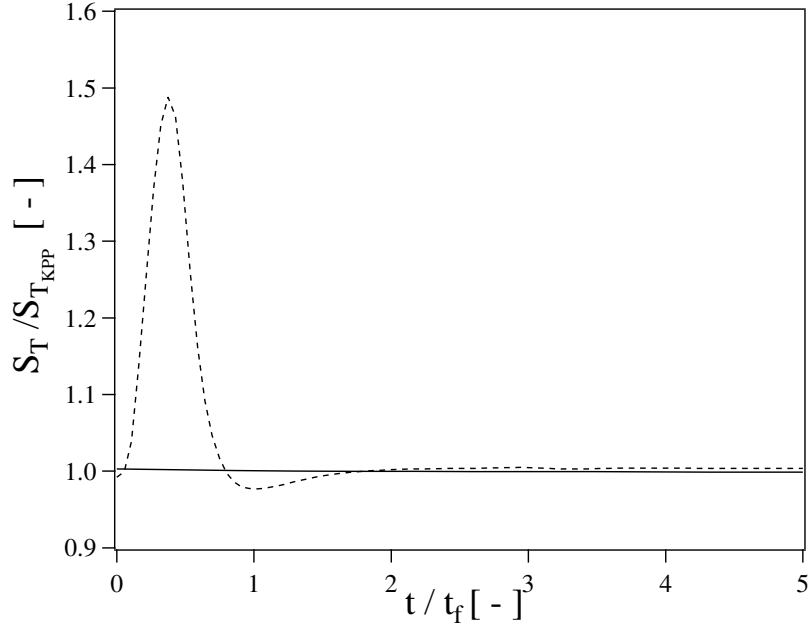


Fig. 3. 1D laminar and turbulent flame propagation. Convergence of the computed flame speed towards the theoretical KPP flame speed for the laminar case ($S_{T_{KPP}} = S_l$) (—) and the turbulent case (- - -).

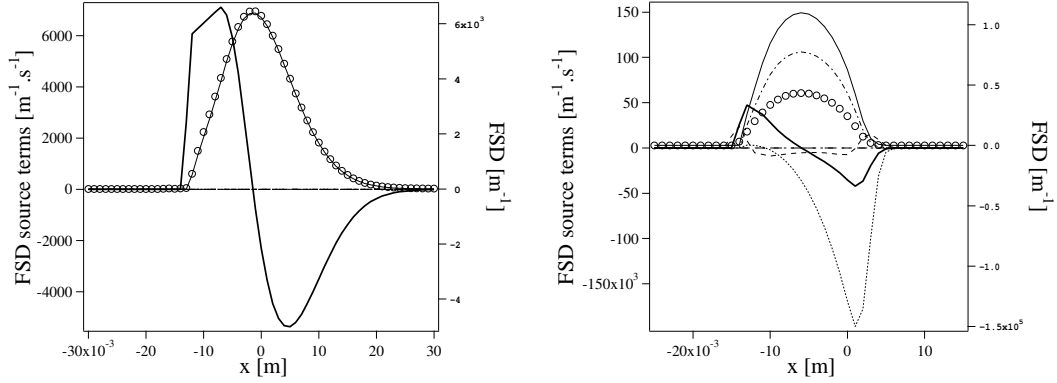


Fig. 4. 1D laminar (left) and turbulent (right) flame propagation. Budget of the FSD equation (Eq. 20): diffusion - - - ; resolved propagation — ; resolved strain rate - - - ; resolved curvature - · - · ; sgs strain rate - · - · ; sgs curvature · · · · · . Correspondence between FSD (—) and $|\nabla\tilde{c}|$ (○) (Eq. 24).

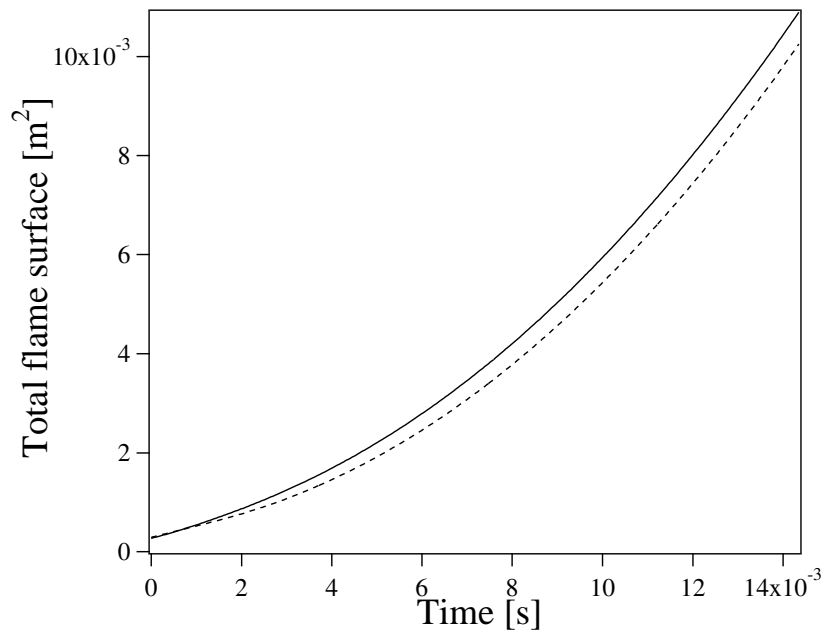


Fig. 5. Spherical laminar flame expansion. Theoretical (—) and computed (---) flame surfaces.

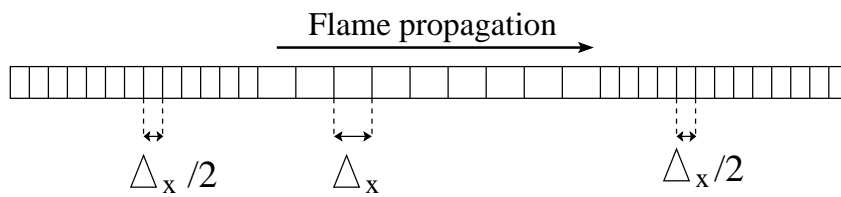


Fig. 6. Schematic representation of the non-regular mesh.

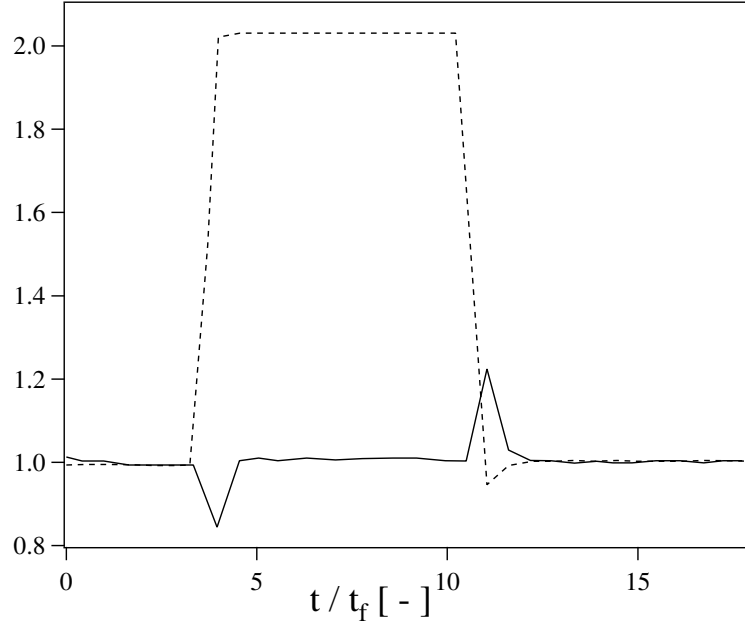


Fig. 7. Propagation on a non-regular mesh. Flame speed $S_T/S_{T_{KPP}}$ — ; flame thickness $\delta_l/\delta_l(t=0)$ - - - .

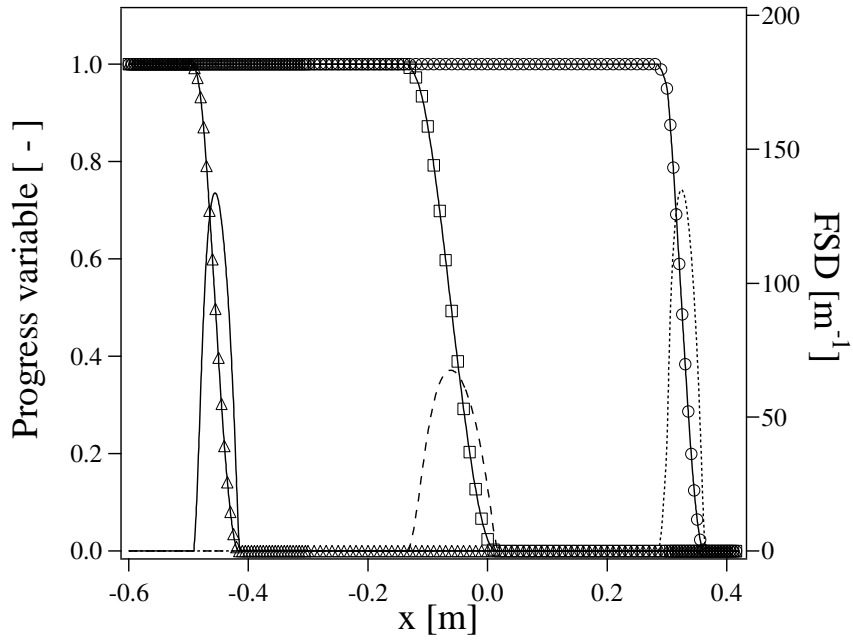


Fig. 8. Propagation on a non-regular mesh. Flame front resolution at different instants: FSD ($t/t_f = 3.0$ — ; $t/t_f = 8.4$ - - - ; $t/t_f = 12.5$ ·····) and \tilde{c} profiles ($t/t_f = 3.0$ — \triangle — ; $t/t_f = 8.4$ — \square — ; $t/t_f = 12.5$ — \circ —).

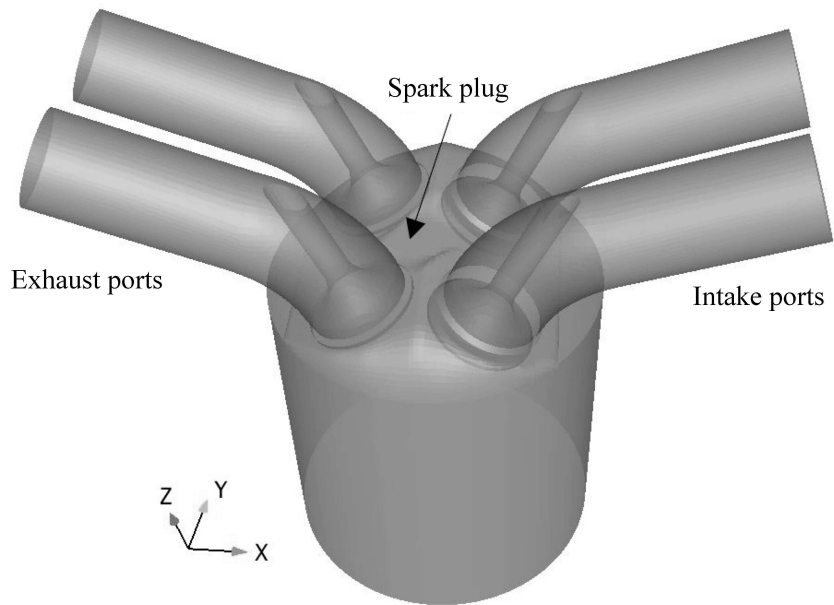


Fig. 9. View of the four-valve SI XU10 engine.

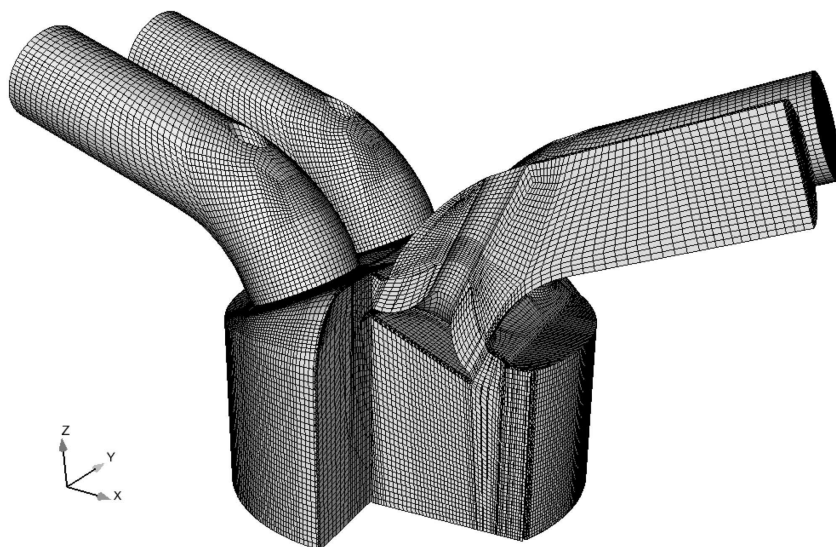


Fig. 10. Computational mesh 70 CAD after intake valve opening.

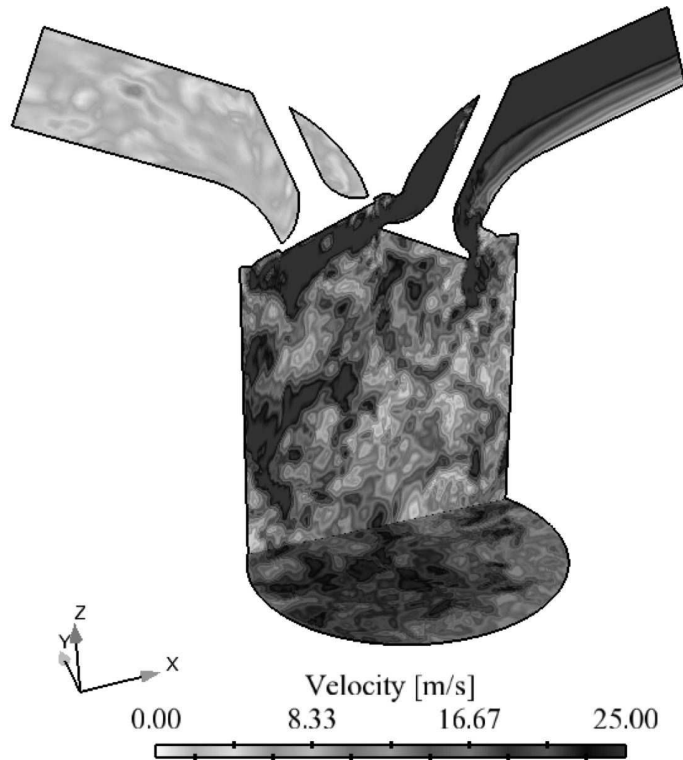


Fig. 11. Velocity magnitude field at 1225 CAD (cycle 3, 140 CAD after intake valve opening).

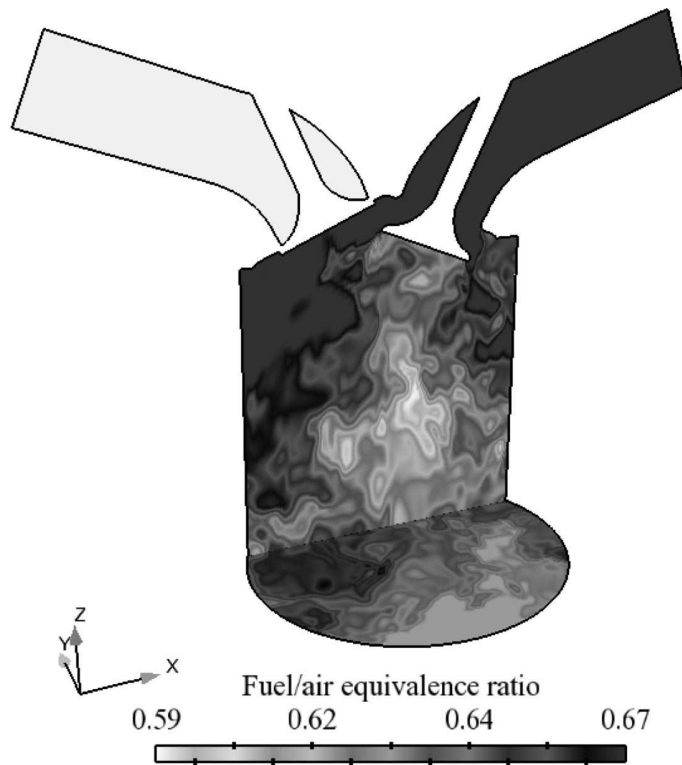


Fig. 12. Equivalence ratio field at 1225 CAD (cycle 3, 140 CAD after intake valve opening).

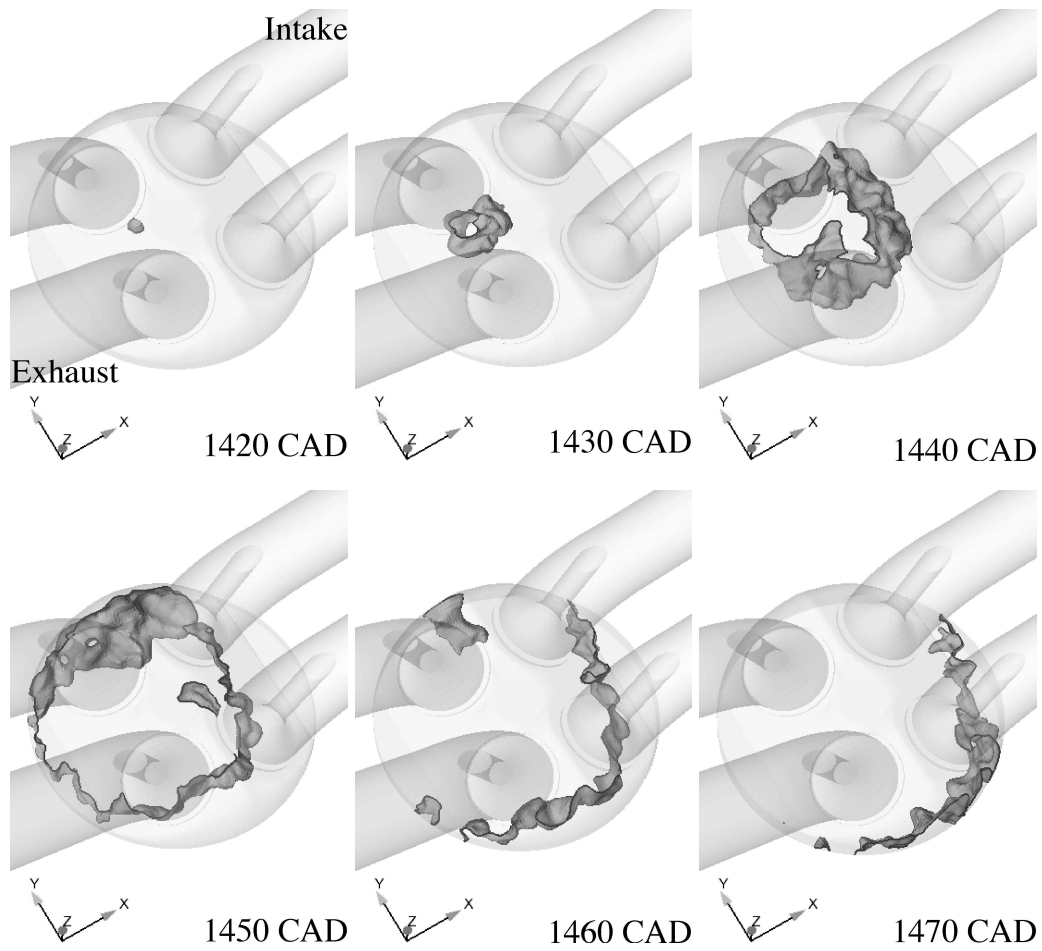


Fig. 13. Iso-surfaces of progress variable ($\tilde{c} = 0.5$) for six increasing times. The crank angle 1440 corresponds to the combustion TDC for the third cycle.

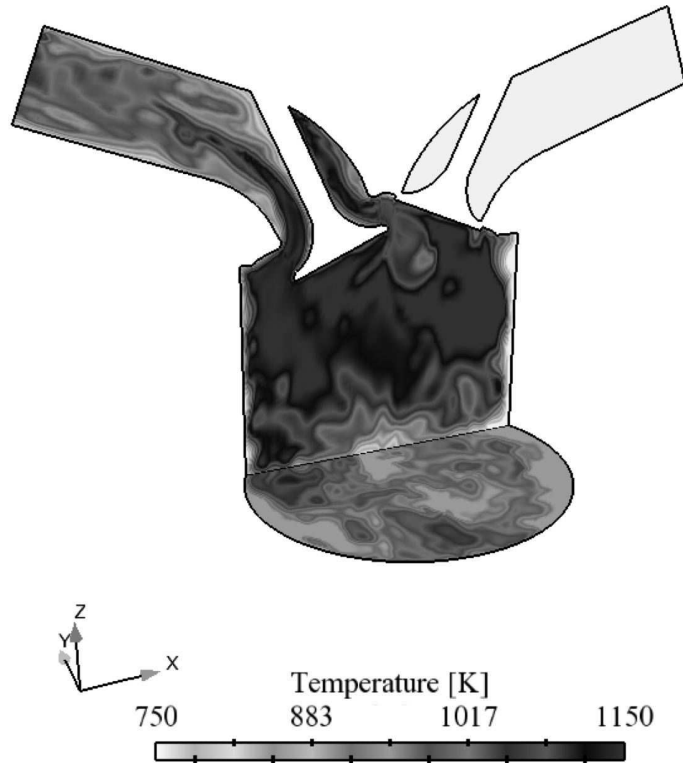


Fig. 14. Temperature field at 1700 CAD (cycle 3, 117 CAD after exhaust valve opening).

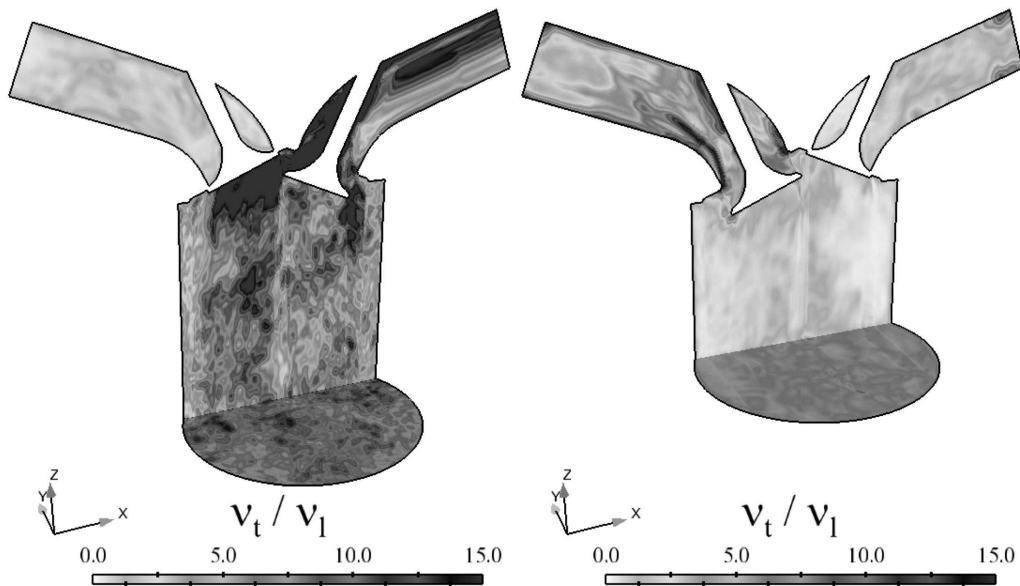


Fig. 15. Subgrid scale viscosity normalised by fluid viscosity at 1225 CAD (left) (cycle 3, 140 CAD after intake valve opening) and 1700 CAD (right) (cycle 3, 117 CAD after exhaust valve opening).

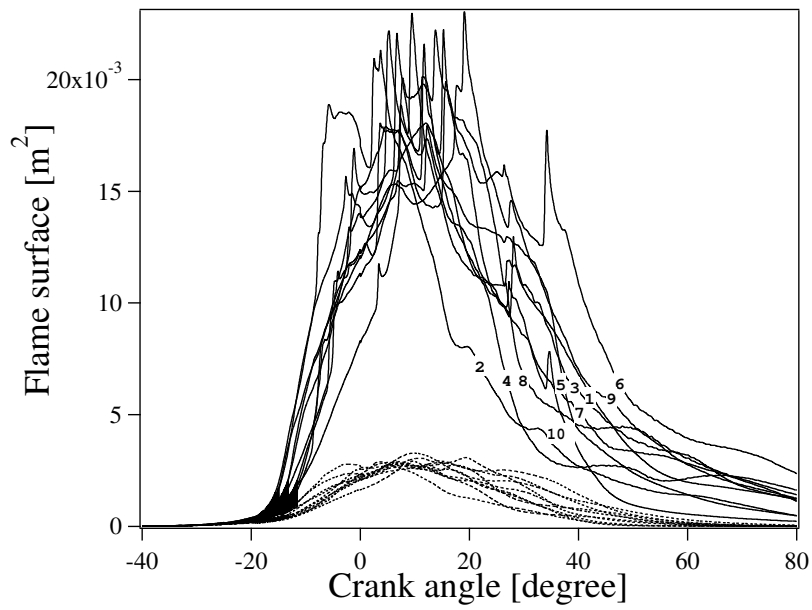


Fig. 16. Evolution of total (—) and resolved (- - - - -) flame surface for the ten LES cycles. Curves are numbered according to the cycle they refer to.

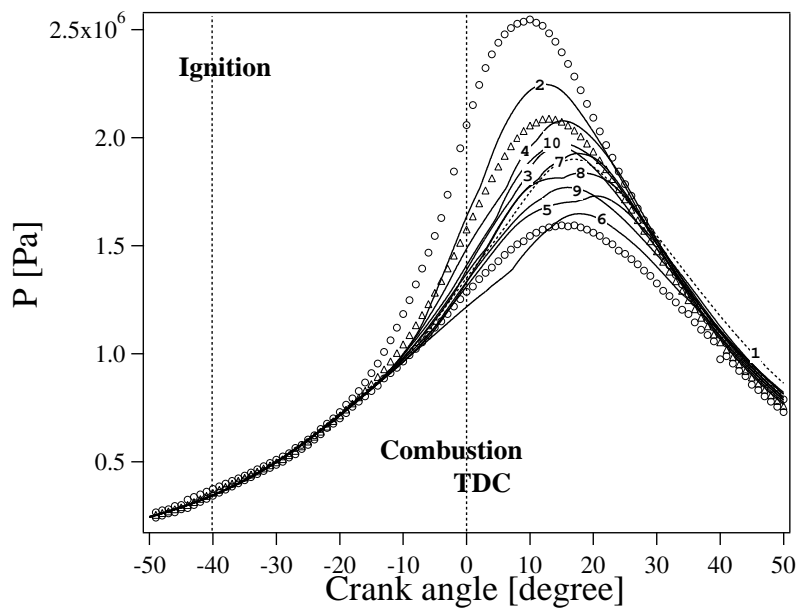


Fig. 17. Evolution of cylinder pressure for the ten individual consecutive LES cycles (first cycle: - - - - - ; nine following cycles: —). Comparison with experimental data: pressure envelope \circ ; phase averaged mean pressure \triangle .

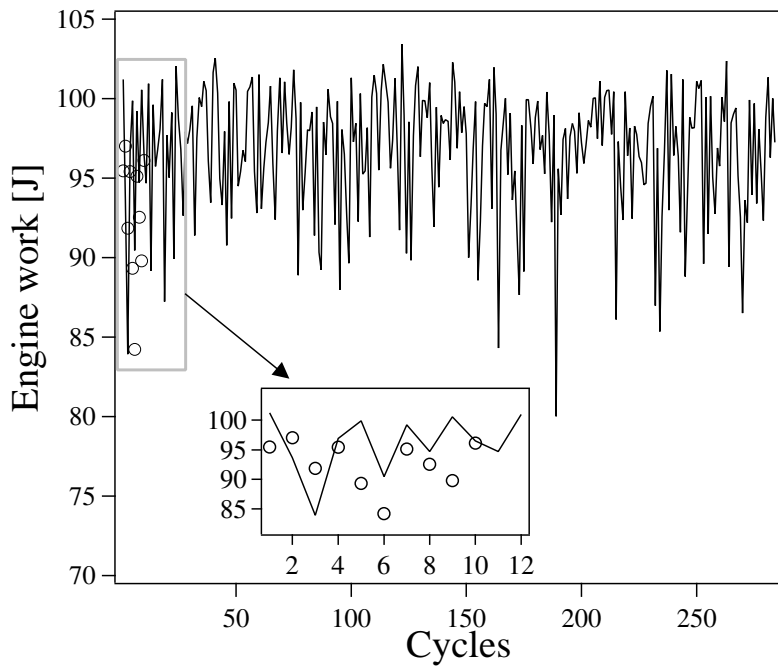


Fig. 18. Engine work computed between 50 CAD before TDC and 50 CAD after TDC. Experimental cycles — ; LES cycles \circ .

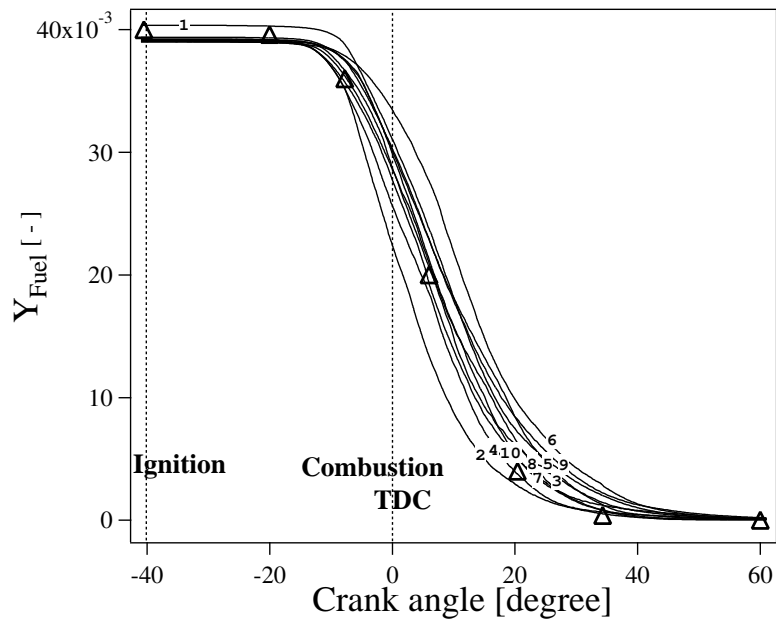


Fig. 19. Evolution of fuel mass fraction for the ten LES cycles (—). Comparison with experimental mean value (Δ).

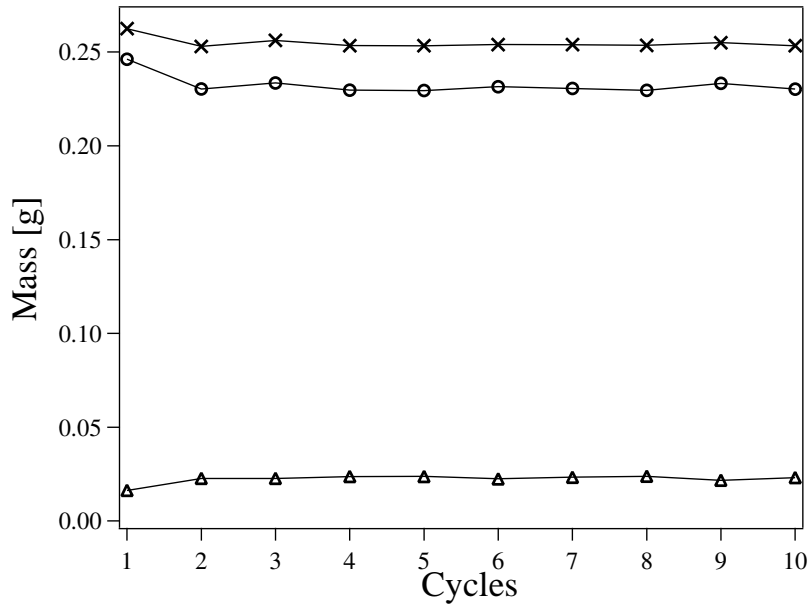


Fig. 20. Total trapped mass (\times), fresh gases mass (\circ) and residual gases mass (Δ) in the cylinder for the ten LES cycles.

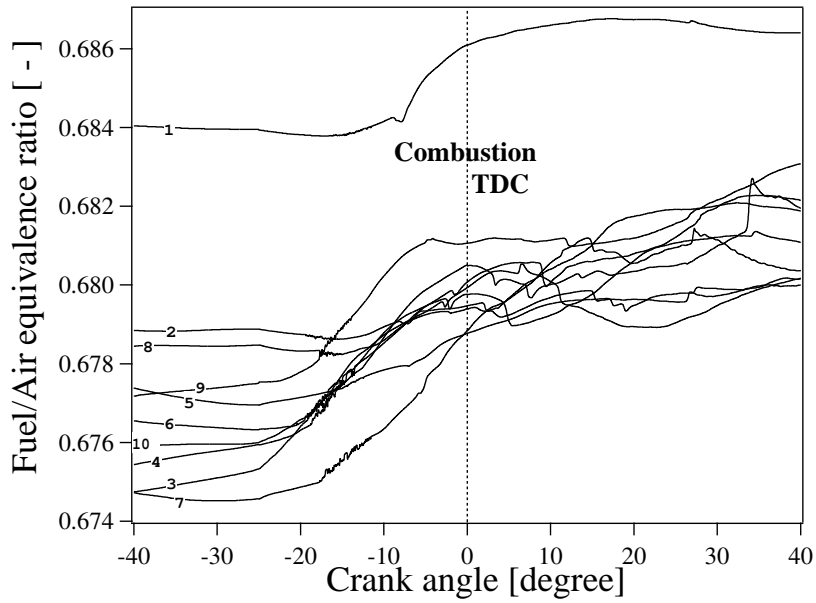


Fig. 21. Evolution of fuel/air equivalence ratio conditioned on the flame surface $\langle \phi \rangle_{\Sigma}$ for the ten LES cycles.

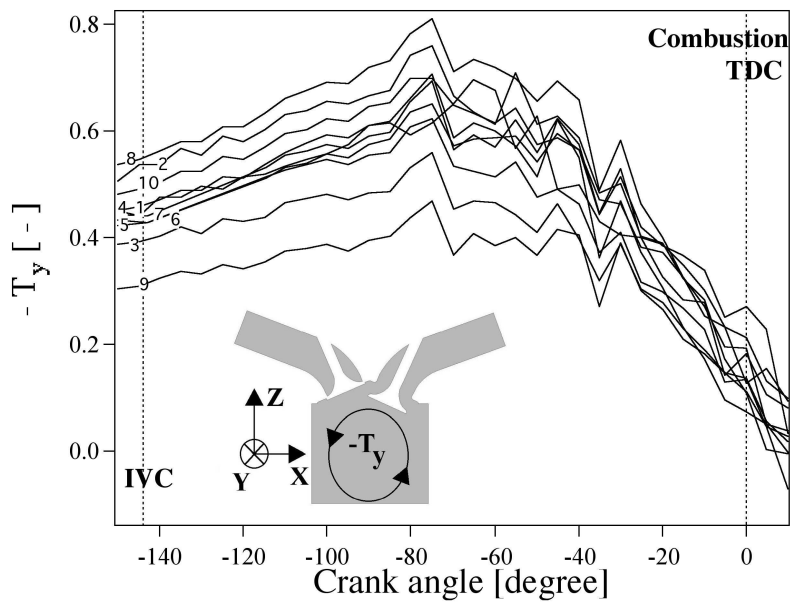


Fig. 22. Tumble ratio about y-axis during the compression stroke for the ten LES cycles.

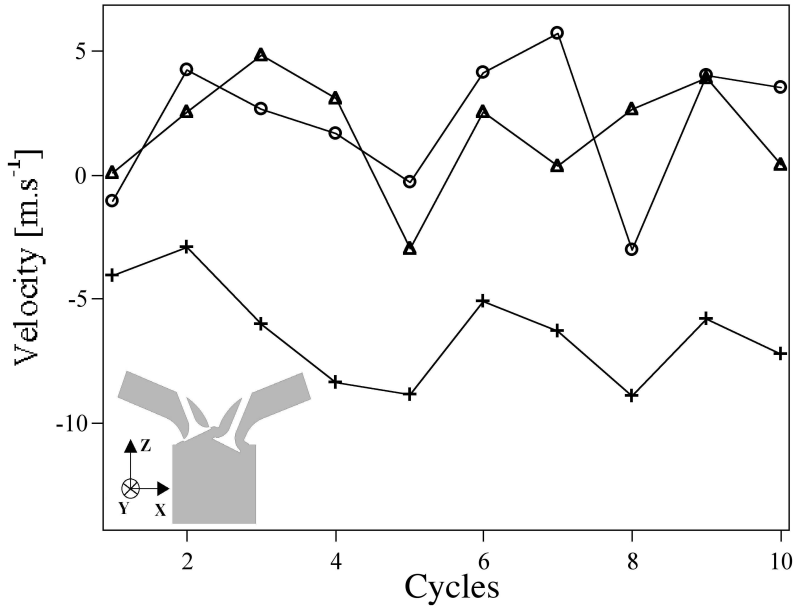


Fig. 23. Resolved flow velocity components in the spark plug vicinity at spark timing for the ten LES cycles; x-velocity: + — +; y-velocity: o — o; z-velocity: Δ — Δ.

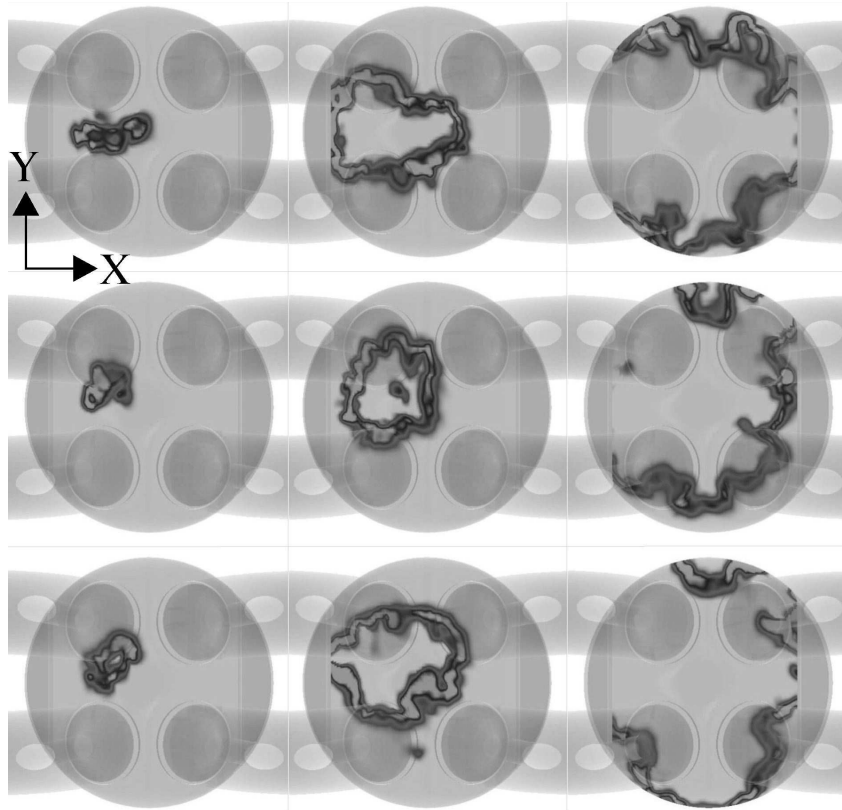


Fig. 24. FSD fields at three instants in cutting planes located just under the spark plug. Exhaust ducts are on the left, intake ducts on the right. Top row: cycle 5; middle row: cycle 6; bottom row: cycle 7. From left to right: 10 CAD before TDC, TDC, 20 CAD after TDC.

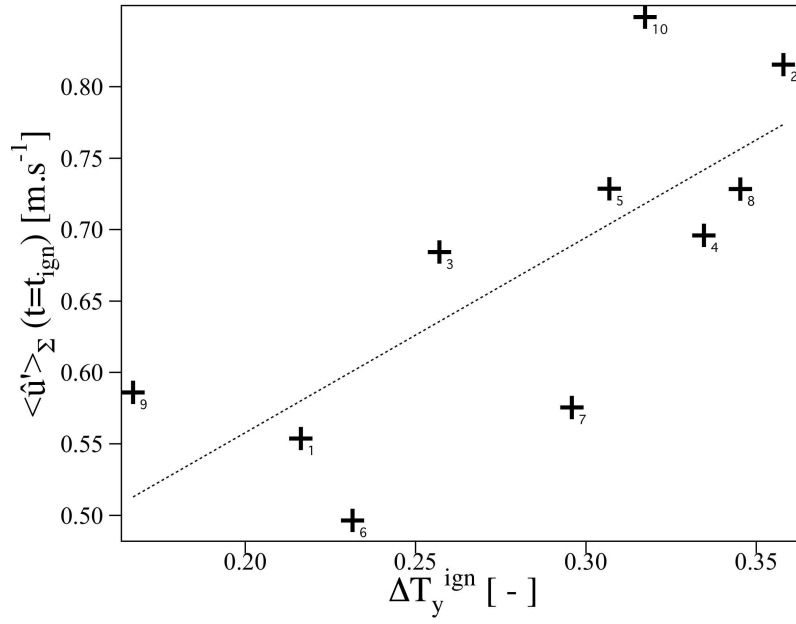


Fig. 25. Correlation between sgs turbulent velocity at the flame front $\langle \hat{u}' \rangle_{\Sigma}$ and tumble ratio drop at spark timing ΔT_y^{ign} .

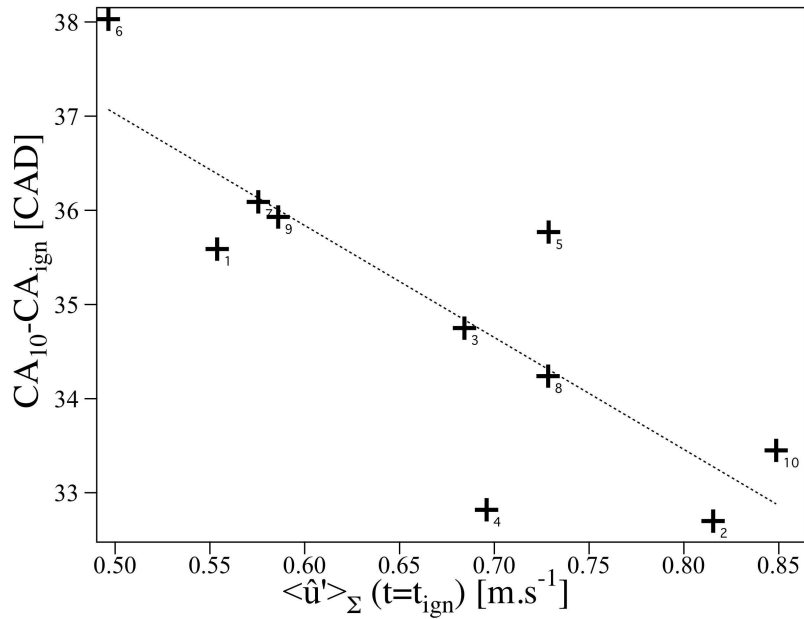


Fig. 26. Correlation between combustion duration $CA_{10} - CA_{ign}$ and sgs turbulent velocity at the flame front $\langle \hat{u}' \rangle_{\Sigma}$ at spark timing.

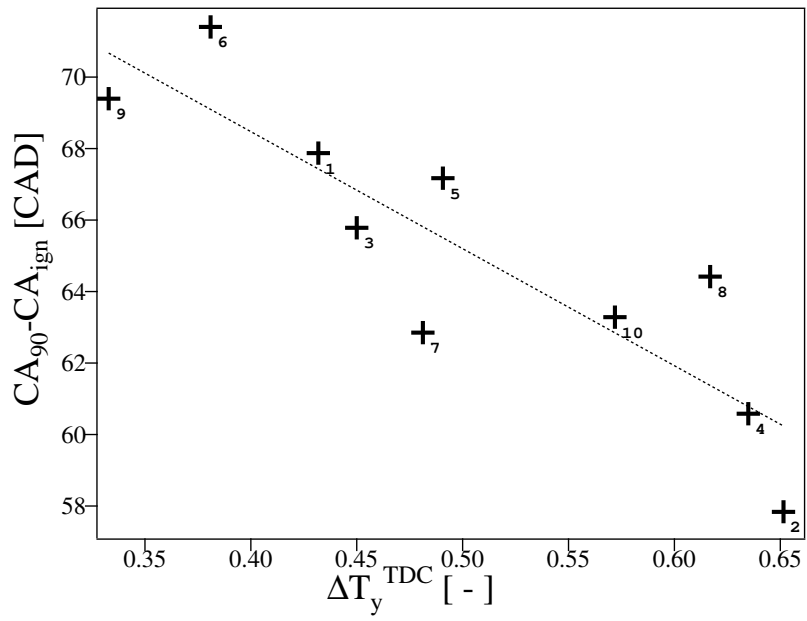


Fig. 27. Correlation between global combustion duration $CA_{90} - CA_{ign}$ and overall tumble ratio drop ΔT_y^{TDC} during the compression stroke.